EARLY SINKHOLE DETECTION AND CHARACTERIZATION IN WEST-CENTRAL TEXAS USING INSAR TIME SERIES AND ELECTRICAL RESISTIVITY TOMOGRAPHY

By

Yosef Darge

Bachelor in Geoinformatics

Adama Science and Technology University

Adama, Ethiopia

&

Master of Science in Remote sensing and GIS

Addis Ababa University

Addis, Ethiopia

Submitted to the Graduate Faculty of

the College of Science and Engineering

Texas Christian University

in partial fulfillment of the requirements for the degree of

Master of Science

May 2023

EARLY SINKHOLE DETECTION AND CHARACTERIZATION IN WEST-CENTRAL TEXAS USING INSAR TIME SERIES AND ELECTRICAL RESISTIVITY TOMOGRAPHY

By

Yosef Darge

Approved by:

DocuSigned by:
Esayas Gebremichael
0D281D746370435...

Dr. Esayas Gebremichael

DocuSigned by:
John Holbrook
36BFE983056E4C4...

Dr. John Holbrook

DocuSigned by:
Mohamed Ahmed
777DE12C577249C...

Dr. Mohamed Ahmed

For the College of Science and Engineering

ACKNOWLEDGMENTS

I would like to begin by expressing my deepest gratitude to God giving me the strength, courage, and guidance throughout this journey.

I would like to say special thank you to my thesis advisor Dr Gebremichael, for his invaluable guidance, expertise, and patience throughout the entire research process. His insightful feedback, critical suggestions, and encouragement have been vital role in completing my research and writing. I also would like to thank my thesis committee members Dr. Holbrook and Dr. Mohamed for their support and feedback to make the project a success.

I am also deeply thankful to the Geology department and all its member's staff who generously shared their knowledge and expertise in the field of geoscience, as well as provided me with valuable resources and opportunities to conduct this research.

I would also like to thank Benite for easing my journey during a challenging time while I adjust to a new environment and culture.

I express my gratitude to my loved ones and friends who provided me with unwavering support and encouragement, particularly to my wife Tigist, who prayed for me throughout the time of my research.

May the Almighty God richly bless all of you.

TABLE OF CONTENTS

LIST OF FIGURES

LIST OF TABLES

CHAPTER ONE

INTRODUCTION

1.1 Research roadmap

This study is aimed at improving our understanding of the processes and triggering factors that induce sinkholes and the early detection of their occurrences in several counties of the west-central region of Texas. The area has experienced significant sinkhole formation primarily due to the presence of soluble rocks coupled with excessive exploitation of natural resources. This phenomenon has adversely impacted critical infrastructures, and the groundwater resource has also been significantly affected. This study used various analytical techniques to detect existing sinkholes, identified new ones, and understand their formation. The outcomes of this study are crucial in implementing suitable mitigation measures to minimize the impact on key infrastructure damage and aquifer contamination.

This study is structured into five major chapters, with the first chapter serving as an introduction to the topic of sinkholes. Within this chapter, a comprehensive background on sinkholes is presented including the different types of sinkholes, and a review of the various datasets and methodologies that have been employed in previous studies to map, quantify, and characterize these sinkhole geological hazards. Additionally, the chapter outlines the objectives of the study and discusses its overall significance.

Chapter 2 of this study presents a detailed overview of the study area, including its geographic location, boundaries, climate, and hydrogeological characteristics of the study area is provided, along with a thorough description of the regional and local geological units.

Chapter 3 provides detailed information on the data sets and methodologies utilized for identifying and characterizing sinkholes. It explains how precursor deformation was analyzed to detect active sinkhole deformation in West Texas. The chapter also outlines a methodical approach to determining the underlying causes and factors that contribute to sinkhole formation by integrating various data sets and assessing their spatial relationships. Furthermore, the chapter describes the software and techniques utilized, along with the data collection campaigns conducted to validate and calibrate the findings.

Chapter 4 focuses on the results obtained from analyzing different datasets through various techniques, individually and in combination. Each method's outcomes and interpretations are presented separately, and the cumulative impact and significance of these interpretations are examined. The chapter highlights the importance of utilizing various datasets and approaches to comprehend sinkholes and the factors that facilitate their development comprehensively. The final chapter (Chapter 5) summarizes the findings of the study.

1.2 Background

Sinkhole is a ground deformation process that is characterized by the downward sinking of earth materials in circular (mostly), linear, or irregular failure patterns (United States Geological Survey (USGS), 2018). Natural processes, such as compaction subsurface erosion and climate events, and human-induced processes are credited for altering the subsurface conditions that contribute to the instability of earth ground conditions causing subsidence (Emil et al., 2021; 2018; Ng et al., 2015; Waltham, 2008). I

Sinkholes are known for their closed topographic depression morphology, and their size/diameter and depth range from a few meters to more than 100 m (Zumpano et al., 2019;

Waltham, 2008). These features are common in soluble rocks, including carbonate rocks such as limestone and dolomite; metamorphic rocks that are easily dissolvable by water such as marble; and evaporite sedimentary rocks that are dominated by salt, anhydrite, and gypsum. Processes that form sinkholes begin when freshwater, or that has become acidic when carbon dioxide is dissolved in it, interacts with the easily dissolvable geologic units. The dissolution rate of the soluble rocks in general primarily depends on the composition of the units, the type of water the units are exposed to (freshwater or acidic water), hydrodynamics (static or moving water, rate of flow, etc.), and the degree of saturation of the solvent with respect to gypsum, salt, or calcite (Martinez et al., 1998; Salvati & Sasowsky, 2002; Waltham, 2008; White, 1984) For instance, the intensity and rates of dissolution are much more rapid in the evaporite rocks exposed to rapidly-flowing waters undersaturated in dominant salts (e.g., sodium chloride (NaCl)), as a result of the composition of the units and their low mechanical strengths, in comparison to carbonate units that come in contact with freshwater. Though the rate is not as rapid as evaporite rock dissolution, carbonate dissolution is amplified when the units are exposed to acidic water (carbonic acid (H_2CO_3)). In such cases, the carbonic acid reacts with the carbonate units to form calcium bicarbonate that easily dissolves in water (Benito et al., 1995; English et al., 2020; Gutiérrez et al., 2008; Hyndman & Hyndman, 2016; Shi et al., 2019; Waltham, 2008).

Sinkholes are classified into many types depending on their morphology and the processes that lead to their formation (Figure 1) (Keller et al., 2016; United States Geological Survey (USGS), 2018)). Solution (dissolution) sinkholes form on solid rocks by a process where (acidic) water seeps into the ground through fractures, faults, and cracks, causing the wall to dissolve causing ground instability and subsidence (Figures 1a). Direct contact between exposed carbonate/evaporite surfaces and water, especially in depressions, also gradually leads to the

formation of solution sinkholes. Other classes of sinkholes include cover-subsidence and cover collapse, often referred to simply as collapse sinkholes. The former develops in terrains overlain by loose and permeable sediments, such as sand, and underlain by soluble rocks (Figure 1b). The mechanism of formation of the cover-subsidence sinkholes is partly similar to the dissolution sinkhole but differs in that the process occurs underneath a permeable layer. It involves the downward settling of the overlying sediments into cavities due to a lack of basal support forming a sinkhole. Collapse sinkholes, the focus of the present study, represent brittle deformation processes formed in terrains overlain by solid rocks or a significant amount of clay in which surface or near-surface material collapses into an underground cavern (Figure 1c). These are the most catastrophic of all sinkhole types (Gutiérrez et al., 2008; Hatheway, 2005; Keller et al., 2016; Nam et al., 2020).

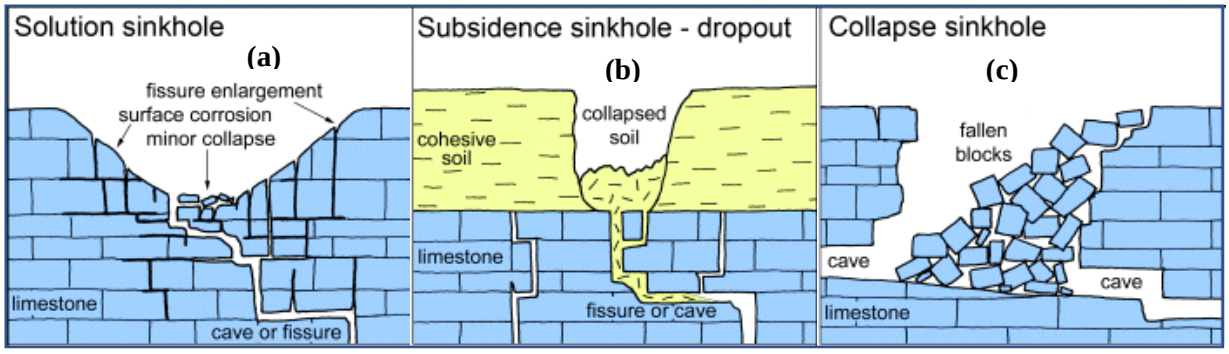

Figure 1: Types of sinkholes – solution (a), cover subsidence (b), and collapse (c) (modified after Waltham (2008)).

As discussed above, sinkholes can form through natural processes such as changes in the characteristics of the surface water (e.g., from fresh to acidic) that comes into contact with the rocks, as is the case for solution sinkholes (Figure 1a), erosional processes, water table fluctuations during drought and extreme flooding, etc. Most of these features that are formed through natural processes are largely prehistoric and do not have a significant impact on inducing hazards with devastating ramifications (Hatheway, 2005). On the other hand, human activities are largely

credited for facilitating the formation of the majority of hazardous sinkholes, particularly collapse sinkholes (Hatheway, 2005; Shi et al., 2019; Youssef et al., 2015). The leading human activities that induce processes that eventually lead to the formation of sinkholes include excessive abstraction of groundwater and oil and gas resources, wastewater injection into the subsurface, poor construction/engineering designs that cause water leakage in underground pipelines, dewatering and underground excavations for mining operations, and land use/land cover changes. Groundwater, in particular, has two contrasting roles in sinkhole forming processes. Firstly, groundwater induces dissolution processes when it comes into contact with carbonate and evaporite subsurface units. However, groundwater also provides hydrostatic pressure that prevents the overlying mass from collapsing (Aydan et al., 2015; Newton, 1987). A decline in groundwater tables as a result of excessive groundwater pumping rates detracts the mechanical support provided to the overburden sediments, which overlie groundwater-saturated cavities generated by the dissolution process, by the groundwater fluid pressure. This in turn results in a vertical downward strain which induces subsidence (sagging) processes (Figure 2) (Ali & Choi, 2019; Frumkin et al., 2015; Khanlari et al., 2012; Xiao et al., 2018). Though subsidence processes, in general, are usually slow, gradual, and imperceptible processes that may not pose significant hazards instantly (Gebremichael et al., 2018), they could also transition to faster deformation rates leading to an abrupt ground failure forming the sinkhole features (Heidari et al., 2011; Yang et al., 2022).

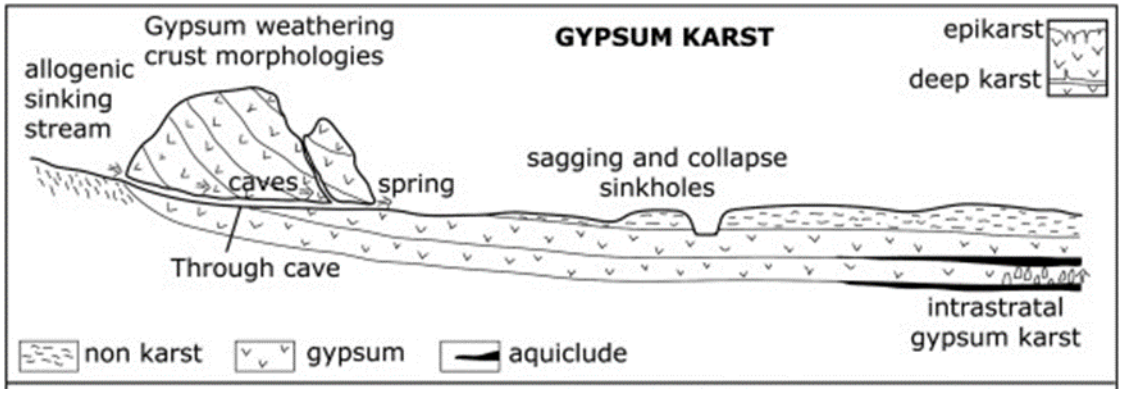

Figure 2: Subsidence (sagging) and sinkhole formation in gypsum terrain (modified from Gutiérrez et al., 2014)

The effect of the groundwater decline is not restricted to the well where groundwater is withdrawn at a higher discharge rate. This is because of the fact that the lowering of the water table leads to the development of the cone of depression around the well (Figure 3). The impact of the excessive groundwater withdrawal on the surrounding areas within the extent of the cone of depression, with respect to facilitating the sinkhole formation process, depends on several factors including the magnitude of the head drop (increased hydraulic gradient) towards the center of the cone of depression that could facilitate internal erosional processes, the nature of the subsurface geologic units, and variations in aquifer parameters such as porosity and permeability (Figure 3) (Alrowaimi et al., 2015; Giuseppe & Pietro, 2021; Xiaoet al., 2020).

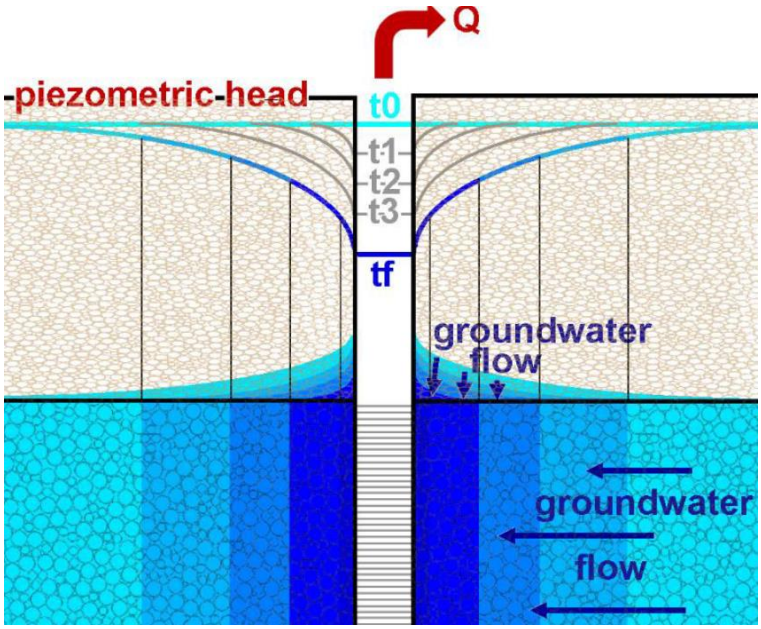

Figure 3: Cone-shaped piezometric head declines over time from the initial time (t0) level to the final time (tf) (Giuseppe & Pietro, 2021)

The occurrence of sinkholes is a major challenge to human lives, infrastructure, and the environment in areas in almost all the states of the United States underlain by soluble rocks. States such as Florida, Oklahoma, Texas, Alabama, Missouri, Kentucky, Tennessee, and Pennsylvania are particularly much more prone to the hazard and have experienced some of the most severe damages as a result of the sinkhole hazards (Kuniansky et al., 2016). Most of the carbonate karst features in the United States are spatially concentrated in the humid parts of the eastern and Pacific coastal parts where the prevalence of evaporite rocks at or near the surface is rare (Figure 4). On the other hand, most karst features in the semiarid and arid areas of the United States are formed as a result of the dissolution of evaporite rocks rather than carbonates due to low precipitation (Figure 4). The total coverage of areas underlain by evaporite rocks amounts to approximately 35 – 40 percent of the total area of the continental United States (Johnson, 2005; Weary & Doctor, 2016).

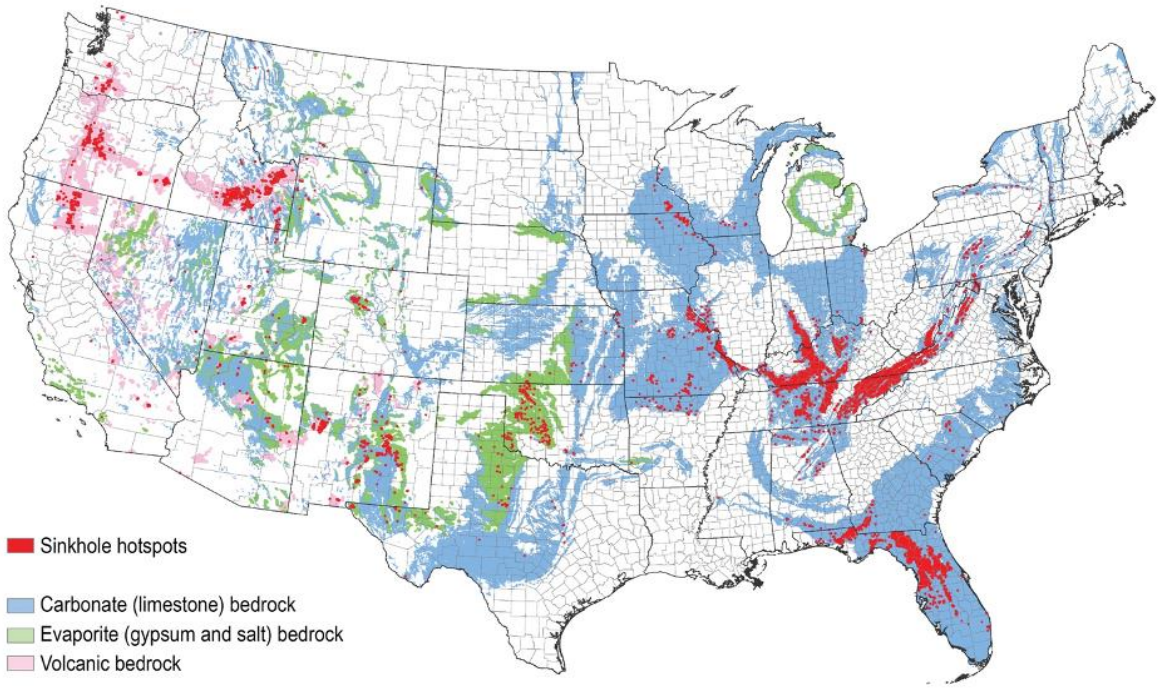

Figure 4: Spatial distribution of carbonate and evaporite rocks across the United States. Also shown (in red) are reported sinkhole incidents (USGS, 2020)

Significant parts of the State of Texas, which are underlain by evaporites and carbonate rocks, are prone to sinkhole hazards some of which have experienced several catastrophic incidents in the past. Most of these incidents were reported in the northern, west-central, and western parts of the state dominantly underlain by the evaporite rocks (Figure 4) (Paine et al., 2012; USGS, 2020). Some of the most widely known/reported sinkholes in Texas are spatially concentrated in the west Texas area within the Permian sedimentary basin known for its massive oil and gas developing activities amounting to nearly 40% of the United States' overall oil production (Johnson, 2005; Monteiro et al., 2022). For example, two massive collapse sinkholes formed near Winkler County in West Texas in 1980 and 2002, whose cause was attributed to the dissolution of the interbedded salt and anhydrite layers at depth in the Delaware Basin (sub-division of the Permian Basin). Several studies suggest that the formation of these sinkholes was largely driven by anthropogenic activities. Most of these studies credit high groundwater extraction rates, and

activities and operations related to oil and gas exploration (brine well) and mining as the leading causes of the formation of sinkholes (English et al., 2020; Johnson, 1989, 2005; Kim et al., 2019; Paine et al., 2012; Shi et al., 2019). The west-central Texas region (also referred to as the North-Central Plains region), located to the east of the Permian Basin (Figure 5), is another area in Texas that is prone to and experienced sinkhole hazards mainly due to the dissolution of evaporites (primarily gypsum and salt) (Figure 5) (Martinez et al., 1998).

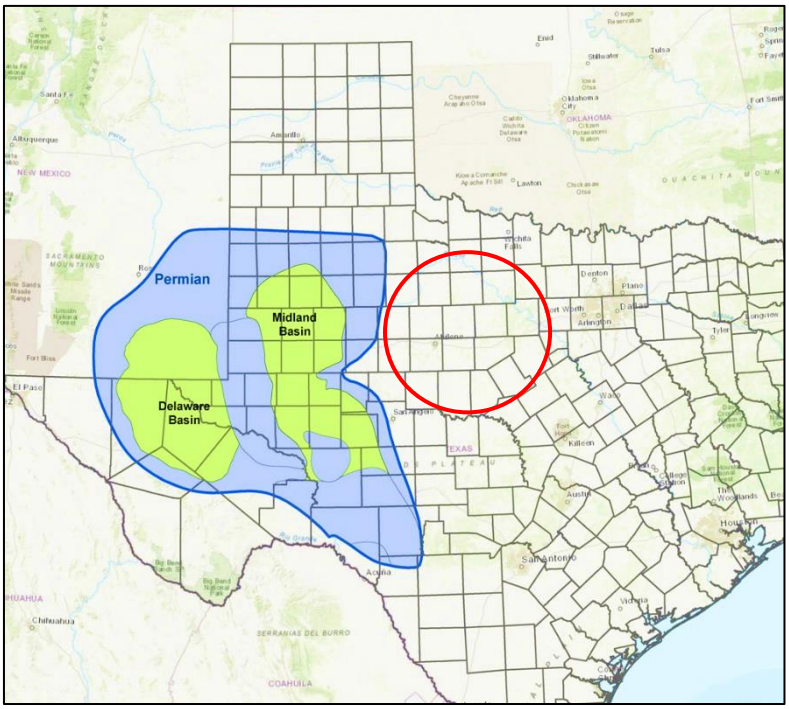

Figure 5: Map of the Permian Basin in Texas and New Mexico. The west-central region is shown in a red circle (modified from https://www.regionsenergyllc.com/).

Unlike the West Texas area, where sinkhole hazards and the processes and controlling factors that induce the hazards were extensively explored in several studies (e.g., Kim et al., 2019), little is known about the spatial distribution of sinkholes/depressions and the underlying processes and factors that give rise to the occurrence of the hazards in the west- and north-central regions of Texas. Determining the spatial distribution and understanding the processes that aggravate the formation of sinkholes will help in developing an early warning system that can be used as input

by the community and policymakers to implement strategies to mitigate the impacts of the hazard. In addition, it will assist policymakers to formulate strategies for sustainable resource management to counterbalance extreme resource utilization practices that were credited for inducing sinkhole hazards in several studies.

1.3 Mapping Sinkholes: Approaches and Limitations

Though sinkholes tend to develop abruptly without any advance warning signs in most instances, precursory processes and their effects such as subsidence and tension cracks can indicate the possibility of the occurrence of the features. Thus, by monitoring the multitemporal progression of the precursory indicators, it is possible to forecast the incidence of sinkhole hazards with some degree of certainty (Carbonel et al., 2014; Deb et al., 2006).

Several studies applied various multidisciplinary approaches to detect, monitor, and characterize sinkhole features. The approaches can broadly be divided into three: (1) analyzing existing sinkholes and controlling factors that induce their occurrence and extending the approach to identify similar sinkhole-like features across the investigated area (Basso et al., 2013; Chen et al., 2018), (2) feature extraction approaches using morphometric parameters (area, perimeter, shape, orientation, and volume), and (3) detecting ongoing (active) sinkhole formation processes by identifying precursory deformation processes (Jones & Blom, 2014; Talib et al., 2022; Theron et al., 2017). Part of the notion behind the first two approaches is that areas containing geometrically and morphometrically similar features to those that had experienced sinkhole incidents in the past are vulnerable to sinkhole hazards in the future. Statistical modeling and probabilistic sinkhole assessment techniques fall under this category. In these techniques, databases/inventory of existing sinkholes, their spatial distributions, and the factors that control their occurrence statistically are integrated to develop statistical, heuristic, and probabilistic

models that could identify areas vulnerable to sinkhole hazards. Analyses techniques falling under the feature detection category include visual interpretation and machine learning algorithms applied on aerial photographs and optical satellite images, and the delineation of depressions using analysis techniques applied on high-resolution Digital Elevation Models (DEM) such as Light Detection and Ranging (LiDAR) datasets in search of sinkhole features. (Benito-Calvo et al., 2018; Hu et al., 2018; Mohammady et al., 2021; Suh & Choi, 2017; Theron & Engelbrecht, 2018). On the other hand, ongoing sinkhole-forming processes are mostly determined by multi-temporal monitoring and quantifying the precursory deformation indicator, namely subsidence, using various methods. These methods employ two main sinkhole observation and monitoring platforms: ground-based (in-situ) and remote sensing. Some of the widely used in-situ methods for monitoring ground subsidence that indicates active sinkhole-forming processes include geophysical, particularly gravimetry, and geodetic monitoring methods. While active sinkhole detection and monitoring tasks using the two methods have produced reasonably acceptable results, their applicability is restricted to monitoring sinkhole-forming processes at a local scale as the methods are costly, labor-intensive, and time-consuming (Closson et al., 2005; Gutiérrez et al., 2011). The synoptic view and repeat observation capability of remote sensing systems offsets this limitation through the provision of multi-temporal datasets capable of monitoring sinkhole precursors over a wide spatial scale (Theron & Engelbrecht, 2018). Though sinkhole detection and precursor monitoring activities using multi-temporal remote sensing datasets have several advantages compared with the in-situ methods as outlined earlier, several sources of errors constrain the accuracy of the results derived using the datasets. These include errors resulting from atmospheric conditions especially on remote sensing datasets acquired from satellite platforms, and geometric and geocoding errors (Al-Kouri et al.,2013; Vajedian & Motagh, 2019). Hence,

sinkhole precursor monitoring tasks should be complemented with in-situ datasets and results, for calibration and validation purposes, to improve the quality and accuracy of the remote sensing-based results (Shi et al.,2019; Emil et al.,2021; Theron et al., 2017). In addition to the geophysical methods that can quantify active surface deformation processes as the gravimetry method does, imaging geophysical methods that could provide a view of the subsurface based on the responses of various layers and features to geophysical signals are widely used to complement sinkhole detection and monitoring operations (Argentieri et al., 2015; Talib et al., 2022).

1.3.1 Mapping Potential Sinkholes

1.3.1.1 LiDAR for Sinkhole Detection

LiDAR uses the two-way travel time of laser pulses sent from sensors onboard aerial (Airborne Laser Scanning (ALS)) or terrestrial (Terrestrial Laser Scanning (TLS)) platforms to ground targets to determine the location and elevation information of the ground surface (Liu, 2008). Although LiDAR data obtained from the terrestrial platforms (TLS) provide high-resolution and detailed ground data that could be used for mapping sinkholes with better accuracy, their limited spatial coverage prohibits their use for mapping features over a wider spatial extent (Gutiérrez et al., 2019). The Airborne LiDAR acquisition system (ALS), henceforth simply referred to as LiDAR, collects information from a sensor, equipped with an inertial measurement unit (IMU) and GNSS positing system, which are installed on a moving or static aerial platform to generate a 3D model of the surface (Figure 6) (Corradetti et al., 2022; Hofierka et al., 2017).

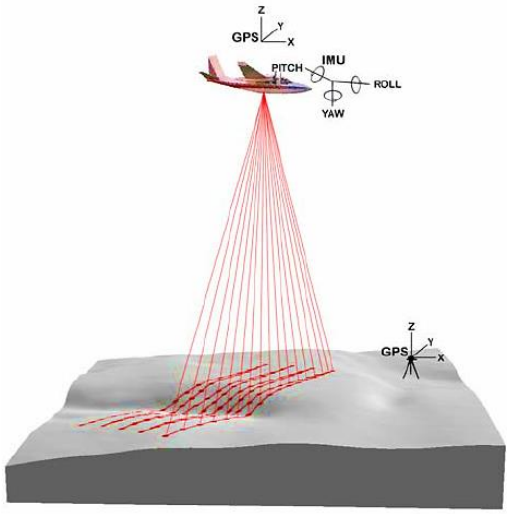

Figure 6: Illustration of airborne LiDAR components and data acquisition (McGaughey et al., 2006)

LiDAR technology has been widely used for various applications, particularly for geomorphological mapping purposes to identify features on the surface of the Earth based on their morphological attributes. Besides the high-resolution terrain information provided by LiDAR data compared with the conventional elevation information obtained from satellite platforms, the ability of LiDAR systems to see through surface cover (such as forests and buildings) and mapping the bare surface make them ideal to identify morphological features that indicate various past or ongoing processes (Doctor & Young, 2017). In recent years, the LiDAR data acquisition technology and the resolution of LiDAR data have significantly improved (as much as to less than one meter), making it possible to detect and map the considerably smaller-sized surface features and allowing scientists to study sinkhole depression distribution and characteristics accurately and realistically (de Carvalho Júnior et al., 2013a; Filin et al., 2006; Seale et al., 2008; Shannon et al., 2019; Zumpano et al., 2019). For instance, Seale et al. (2008) used LiDAR data to identify existing sinkholes in Pinellas County, Florida, by observing the morphologic and geometric characteristics of the features and verifying the accuracy using ground-truthing methods. Other studies demonstrated the ability of point cloud LiDAR data to map the distribution of sinkholes in the

Dead Sea region (e.g., Filin at el., 2006). Similarly, Montane et al. (2001) and Honings et al. (2022) successfully mapped subtle topographic features associated with sinkholes in the southern (Central Florida) and southeastern (Dougherty Plain) United States' karst terrains using LiDAR technology and validating the accuracy through the analysis of ground penetrating radar (GPR) geophysical data (Montane, 2001).

1.3.2 Detecting Active Sinkholes Though Monitoring of Subsidence Precursors

As discussed above, subsidence processes have been identified as key precursory indicators of pre-failure active sinkhole-forming processes and as a result, long-term measurements of surface deformation/displacement rates and identifying areas undergoing subsidence are being used for early identification and monitoring of sinkholes (Intrieri et al., 2015).

1.3.2.1 Global Navigation Satellite System (GNSS)

Permanent or campaign Global Navigation Satellite System (GNSS) measurements are widely used to monitor precursory active deformation processes in suspected sinkhole sites (Kersten et al., 2017). Though the GNSS measurements can quantify subsidence rates with centimeter to millimeter scale precision, their capability to monitor sinkhole processes on a wider scale is limited. This is because GNSS measurements provide point measurements and can only quantify deformation rates at the point where the measurements were recorded (Rodriguez-Lloveras et al., 2020).

1.3.2.2 Interferometric Synthetic Aperture Radar (InSAR*)*

Interferometric Synthetic Aperture Radar (InSAR) techniques applied on Synthetic Aperture Radar (SAR) datasets, acquired by satellite-based sensors, overcome the limitations posed by point-based deformation measurements (subsection 1.3.2.1) by providing deformation rates over a wider spatial scale (Rucker et al., 2013). SAR data comprises two signals that are

equally important for detecting active sinkhole processes: amplitude and phase. InSAR techniques rely on the phase component of the SAR data to measure the fine-scale movement of surfaces over large areas with high temporal frequency. This makes the technology ideal for monitoring sinkholes and other subsidence processes in contrast to time-consuming and labor- and resource-intensive field (in-situ) techniques (Crosetto et al., 2016; Ferretti et al., 2007; Theron & Engelbrecht, 2018).

InSAR uses multi-temporal SAR imagery of a target surface to extract coherent phase differences (R1 and R2 in Figure 7) between two antennas, on the same satellite or acquired during a revisit overpass, to calculate the change in distance between the satellite and the target between observations to measure surface displacements (Hanssen, 2001; Rosen, 2000). An interferogram, generated by cross-multiplying the amplitude information of the two SAR images while differencing the phase information, is expressed in equation (1) (https://site.tre-altamira.com/insar/).

$$\emptyset \boldsymbol{in} = \frac{\boldsymbol{4\pi\ \Delta R}}{\boldsymbol{\lambda}}, \boldsymbol{\Delta R = R1 - R2} \quad \text{. . . . . Equation 1.}$$

Where R1 is the first pass data acquisition, R2 is the second pass data acquisition, and ΔR is the difference between the two acquisitions, while λ is the antenna wavelength, and $\emptyset in$ is the interferogram phase.

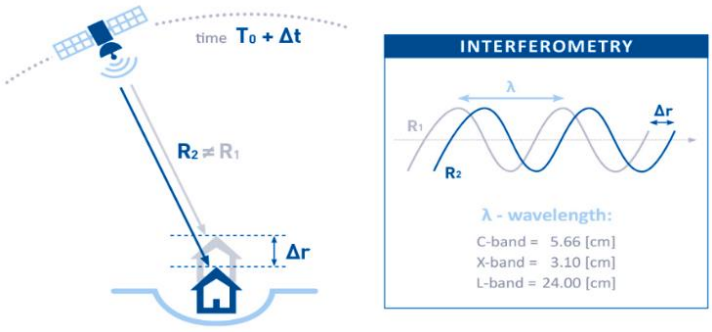

Figure 7: InSAR surface deformation measurement (https://site.tre-altamira.com/)

InSAR techniques have been extensively used for investigating surface deformation processes resulting from various inducing factors and processes. For instance, the technique was used to investigate the deformation pattern of two geothermal areas in West Java, Indonesia. The study used ALOS PALSAR and Sentinel-1A data from 2007 to 2009 and 2015–2016, and an uplift pattern was observed around the injection zone of geothermal areas (Maghsoudi et al., 2018). Similarly, the technique has been successfully applied for the detection and monitoring of sinkholes in West Texas's Permian Basin (Shi et al., 2019). The study applied InSAR techniques on 16 ALOS PALSAR images (acquired from 2007 to 2011) to monitor the subtle gradual deformation of existing sinkholes. It also detected potential sinkholes in an area about 1 km northeast of the existing Wink Sink 2 that exhibited a maximum subsidence rate of up to -40 cm/yr (Shi et al., 2019). In a similar application of InSAR for sinkhole mapping purposes, a study conducted in the Dead Sea, Israel, utilizing the InSAR technique using RADAR data sets obtained from COSMO-SkyMed satellite images revealed that precursory subsidence occurred a few months before the failure of all three existing sinkhole sites in the area (Nof et al., 2013). In another study, Talib et al. (2022) used TerraSAR-X RADAR images to detect precursor sinkhole deformation in West-Central Florida using InSAR techniques. Their results indicated that

subsidence patterns with values ranging from -3 to -6 mm/yr, observed in areas including buildings ranging in size from 300 m² to 2000 m², signify ongoing sinkhole forming processes.

1.3.3 Validating Sinkhole Detection through Geophysical Method

Using subsidence only for identifying depressions that are presumed to be active sinkholes may lead to an erroneous assessment as these measurements alone are not accurate enough to characterize sinkholes without knowing the properties of the subsurface (Intrieri et al., 2015). Ground-based geophysical measurements have been used in a variety of applications to assess subsurface properties, which is critical for investigating an area susceptible to a sinkhole, as they provide a comprehensive view of the subsurface based on the contrast in the responses of the units/layers of the subsurface to the geophysical signals. One of the most widely used near-surface geophysical methods for karst studies is 2D Electrical Resistivity Tomography (ERT) (Stan-Kłeczek et al., 2022). In the ERT surveys (Figure 8), a direct current is injected into the ground through current electrodes, and the potential difference is then measured which will be used to calculate and generate the lateral and vertical resistivity distribution map of the subsurface. Apparent resistivity and pseudo-depth values acquired from the field surveys are processed using inversion software to calculate true resistivity and depth values that reflect actual subsurface conditions (Loke et al., 2013). The variations of resistivity as a factor of the permeability and degree of saturation of the subsurface material are used to detect the presence of sinkhole features as well as determine their geometries (Hussain et al., 2020; Montgomery et al., 2020; Mukhwathi & Fourie, 2020).

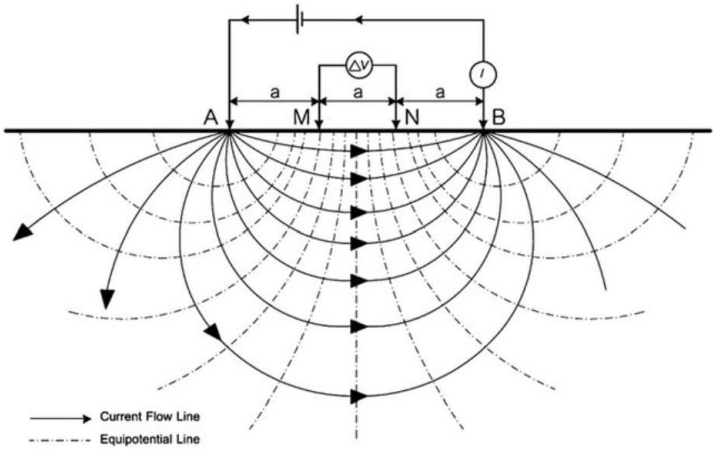

Figure 8: Wenner Array electrode configuration where A and B represent current electrodes while M and N signify potential electrodes. The injected current is shown as 'I' while 'V' and 'a' represent voltage and electrode spacing, respectively (Tesfaldet & Puttiwongrak, 2019; Wiwattanachang & Giao, 2011).

1.4 Statement of the problem

Significant parts of the study area, underlain by evaporite and carbonate rocks, are prone to sinkhole hazards that have caused destructive incidents in the past. For example, a sinkhole recently formed at the intersection of Grape and Franklin streets in north Abilene (Figure 9) which damaged the road and incurred thousands of dollars for repair (Henderson, 2021). As stated above, the study area is undergoing a significant economic transformation driven by significant anthropogenic activities and resource (groundwater, oil, and gas) extraction. These create a conducive setting for the development of gypsum and salt caverns and other karst features over time (Johnson, 2018). Figure 10 demonstrates the spatial zones where recent sinkhole incidents (shown in pink color) in the study area and surroundings have been reported (USGS, 2020). For instance, at least four large areas in Abilene city and surroundings, where there are high population distribution and infrastructure, fall within the area where recent sinkholes have developed (Figure 10). In addition to the areas shown in Figure 10, several recent or past events have been reported in various parts of the study area (Young, 2016). Hence, it is imperative that these features are identified and their mechanism of formation determined to protect the public and infrastructure

from catastrophe induced by the incidence of the hazards. It will also help in preventing the contamination of the groundwater resources that occurs when the groundwater is exposed to contaminants when the overburden is removed as a result of the ground failure (Zhou & Beck, 2008).

Figure 9: A recent (2021) sinkhole that occurred in northern part of Abilene caused significant property damage (Henderson, 2021)

1.5 Research Questions, Objectives, and Significance

In this study, an integrated approach employing remote sensing and in-situ datasets and results derived using analyses techniques applied on the datasets were used for the following key objectives:

- To detect potential sinkhole features and map their spatial distributions by assessing the geometric and geomorphic properties of the surface features and their long-term displacement patterns.
- Identify (define) possible natural and anthropogenic-led processes and factors that induce the formation of the sinkholes and related surface deformation processes.

To attain the objectives of the research, the following research questions were addressed:

- Could morphology and geometric attributes of land surface features be indicative of processes that formed sinkholes and other karst features?
- Can the monitoring of precursory surface deformation indicators be used to determine active sinkholes?
- What are the controlling factors that may influence the formation of sinkholes? what is the role and significance of anthropogenic processes in aggravating the formation of sinkholes?

Though the problems arising from the incidence of sinkholes in the study area have long been recognized, there are no studies to date that have provided conclusive and comprehensive views on the complexity and severity of the problem, the spatial distribution of the features, inducing factors, and potential mitigating measures. This study addressed these gaps and demonstrates the feasibility of using multisource datasets and techniques to develop a sinkhole early-warning system that can avert the destruction caused by sinkholes and suggested mitigating measures to curtail their occurrence.

CHAPTER TWO

STUDY AREA, CLIMATE AND GEOLOGY

2.1. The Study Area

The study area (total area: 15,810 km^2) encompasses parts of Taylor, Fisher, Haskell, Knox, Stonewall, Callahan, Shackelford, and Jones Counties of the west-central region of Texas (Figure 10). It is bounded to the West by the Permian Basin and lies within the Rolling Plains physiographic province of Texas – a subdivision of the North Central Plains (Figure 5). Taylor and Jones counties are relatively densely populated, with a total population amounting to 141,739 and 19,721, respectively. The majority of the dense population distribution of Taylor County is centered in and around the major city in the study area – the city of Abilene (US Census Bureau (http://www.census.gov/)).

2.2. Physiography, Soil, and Climate

The elevation in the study area varies from 397 to 775 m above sea level. The terrain in the northeast and central regions is primarily flat. In contrast, the northwest, southwest, and southeast regions have a slope that gradually rises with the terrain being short and steep in the valley. The topography in the southeast and northwest regions constitutes more complex landforms of ridges, valleys, and more streams than the northeast part of the terrain (Figure 10) (Drees, 1986; Price, 1978).

The primary soil type of the study area is commonly known as the red-colored “Redbed”, which is mostly Permian in age and alluvial and eolian in origin, formed following the weathering and deposition of Permian shales and sediments (Drees, 1986). This soil is deep/stratified with red loam to clay loam soils overlying the sand/sandy loam and shale layers (Drees, 1986).

The study area lies within the humid tropical climate zone/type characterized by its hot and humid summers and moderate temperatures in winter and spring (Saman et al., 1996). The mean annual average temperature ranges from 60^0 to 63^0 F. The highest and lowest temperatures were recorded during the months of August and January, respectively. (Gustavson et al., 1981). The average yearly rainfall in the area is 624 mm with the high rainfall amounts recorded during the spring and fall seasons while short rain episodes occur during the summer months (US Department of Agriculture, 2006; Wood & Blackburn, 1984).

The economy of the area relies heavily on agriculture and oil and gas production, while gypsum and cottonseed oil mills also play crucial roles in generating income and job opportunities. The presence of abundant groundwater has created favorable conditions for large-scale farming, with farmlands accounting for approximately two-thirds of the area. The primary agricultural products cultivated through irrigation include cotton, wheat, grain, sorghum, corn, and peanuts. Indigenous plain grasses, such as hairy grass, buffalo grass, big bluestem, Canada wild rye, and Texas bluegrass, cover most of the rangeland. In addition, cotton and wheat are the predominant agricultural products grown in the area.

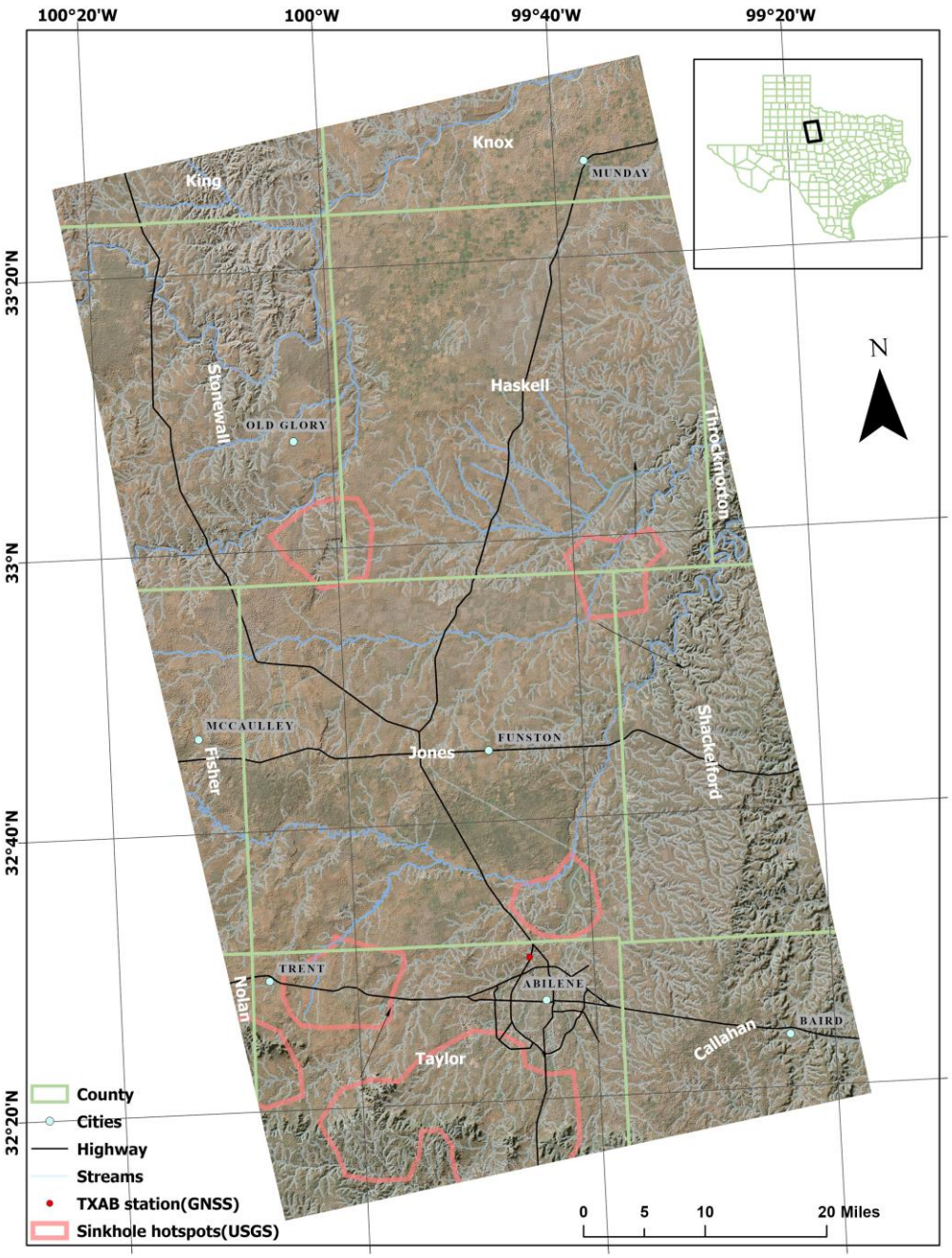

Figure 10: The study area (polygon features marked in pink color are sinkhole hotspot zones (USGS, 2020)).

2.3. Hydrology and Hydrogeology

The watershed containing the study area lies within the Brazos basin, the second largest river basin in Teas, and comprises a sparse network of streams that join major rivers, flowing through the landscape's northeast, north, and northwest valleys, separated by a higher land ridge (Figure 10). The volume of river water largely depends on seasonal precipitation runoff from the surrounding watersheds, which flow into the main water reservoirs of Fort Phantom Hill Lake, Arson North Lake, South Lake, and Lake Stanford (Price, 1978).

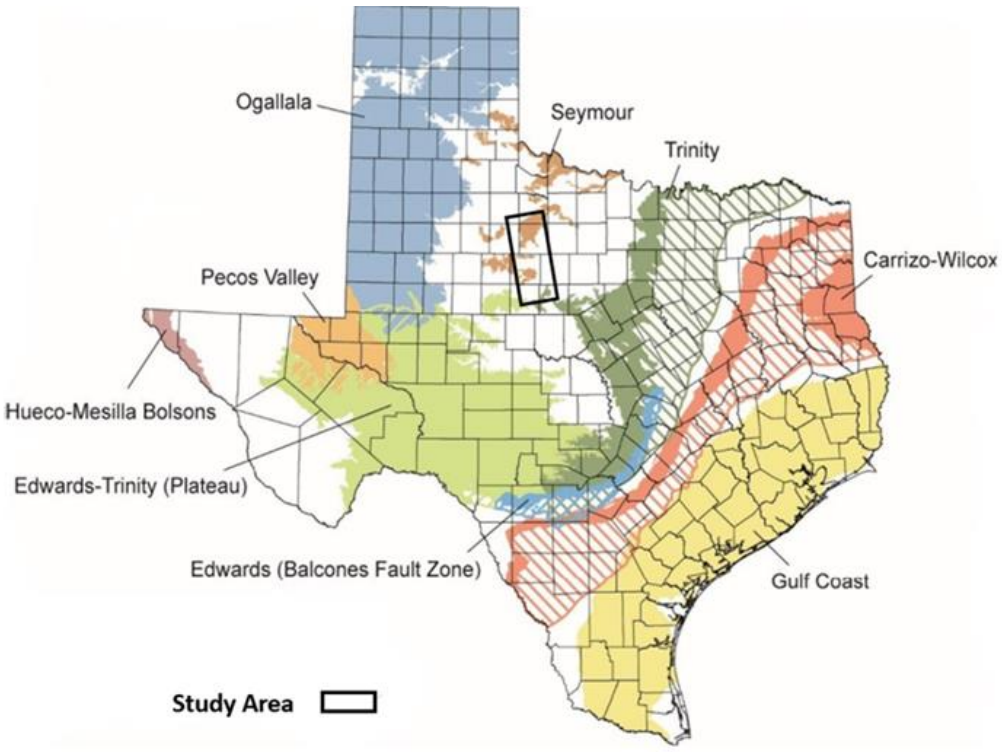

Figure 11: Major Texas aquifers (modified from Bruun et al., 2016). Also shown (in black-outlined polygon is the location of the study area).

The Seymour aquifer (SA) is the major aquifer in the Texas rolling plains region followed by the Edwards-Trinity, Trinity, and (to a lesser extent) the Blain aquifers (Figure 11). The aquifer supplies nearly 85% of the water that is used for irrigated farming in the region (Modala et al., 2017). In addition to groundwater from the SA, minor aquifers are being used for municipal and

industrial purposes accounting for approximately 36% of the total water demand of the region (Bruun et al., 2016).

The investigated area encompasses a significant portion of the SA (Figures 11 & 12). The SA is an unconfined aquifer formed during the Quaternary period by the deposition of unconsolidated and poorly sorted gravel, conglomerate, sand, silt, and clay originating from the High Plains region of Texas and transported via eastward-moving streams. Sediments nearer to the surface exhibit finer grain sizes, whereas those found at greater depths are coarser (Ewing et al., 2004; Harden et al.,1978). Previous studies indicated that the thickness of the SA varies with most areas having a thickness fewer than 100 feet, but few areas do contain as much as 360 feet thick units (Ashworth & Hopkings, 1995; George et al., 2011). The average safe yield pumping rate for the SA is approximately 300 gallons per minute (Sij et al., 2008). According to Chaudhuri & Ale (2014), the SA has higher salinity in some areas, particularly at shallow wells and depths. This was attributed to the unconfined nature of the aquifer that makes it susceptible to various sources of surface contaminants – particularly pollutants emanating from the intensive agricultural activities and practices such as agrochemicals that eventually infiltrate the subsurface and alter the chemistry of the groundwater (Chaudhuri & Ale, 2014).

The study area also contains some parts of the Edward Trinity aquifer, which is one of the major aquifers in Texas but a minor aquifer in the region and the study area (Figure 12). This aquifer extends from the southwest hill of the study area to the southwest of Abilene city covering approximately 281 km^2 (Figure 12). The Edward Trinity Aquifer is a confined aquifer composed of saturated sediments of early Cretaceous age Trinity Group formations and the limestone and dolomite of the Edward Group and sands of the Trinity Group (Bruun et al., 2016; Ashworth & Hopkings, 1995). The aquifer's saturated thickness is generally greater than 100 feet in the study

area and the average yield of the Edward Trinity aquifer is about 50 gal/min (Ashworth & Hopkings, 1995; Bruun et al., 2016).

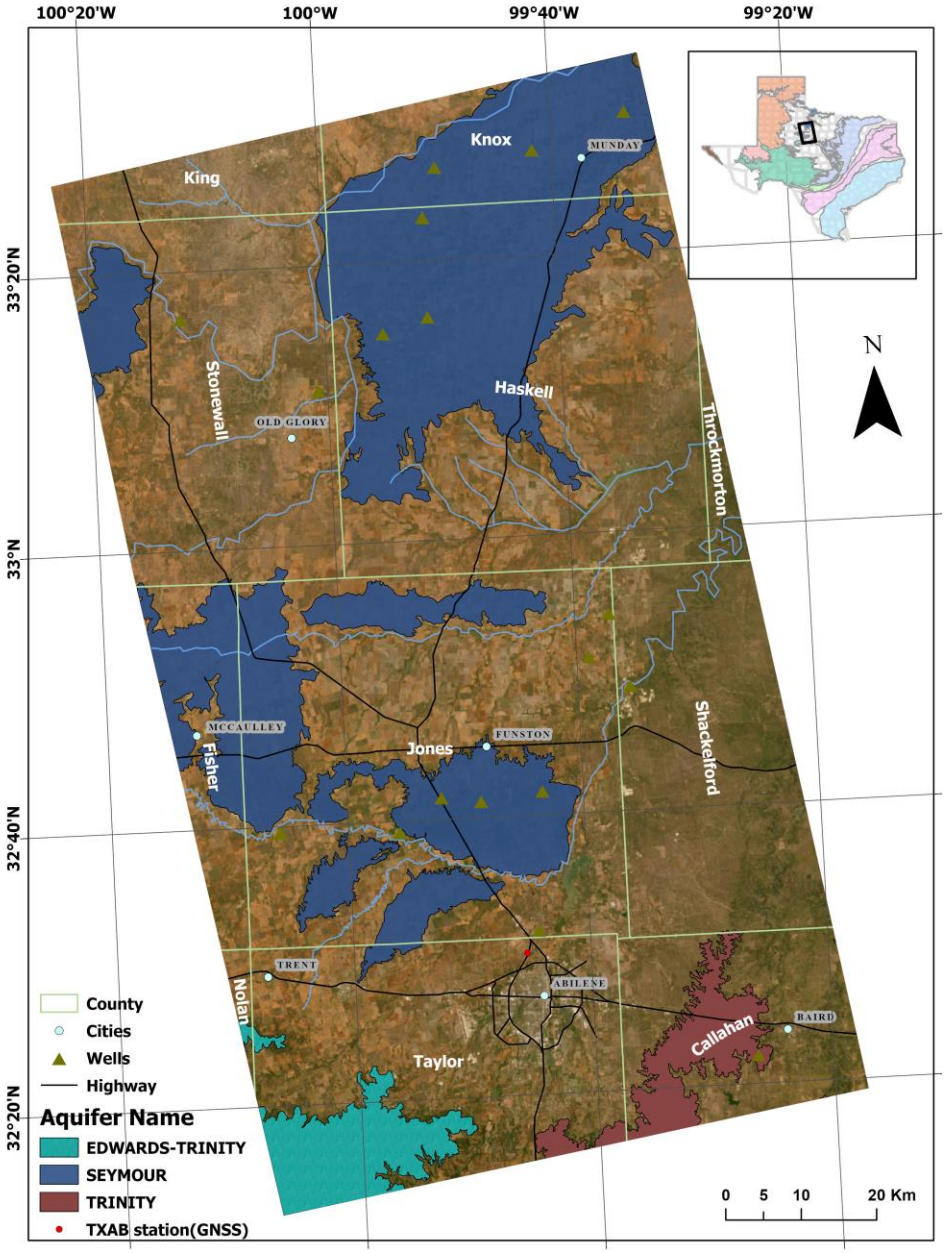

Figure 12: Major aquifers in the study area (the inset map shows the major aquifers of Texas)

The Trinity aquifer, another major aquifer in Texas in general, is only available in limited areas of the study area with a total areal coverage of approximately 232 km^2 (Figure 12). Lithologically, the aquifer consists of limestones, clays, sands, conglomerates, and gravels

(Ashworth & Hopkings, 1995; Bruun et al., 2016). This aquifer's productivity is mainly governed by sand thickness and distribution. The northern Trinity Group has a stratified system of aquifers and aquitards due to the depositional conditions during the Cretaceous Period. Fluvial and coastline water-bearing sandstones were produced as a result of these sandstones' deposition in two different environments (Bruun et al., 2016).

2.4. Geology

2.4.1. Local Geology

Almost all rocks in the Rolling Plains region are sedimentary rocks comprising limestone, clays, shales, sandstones, and conglomerates. The shales and sandstones in various locations are soft and easily eroded by natural processes such as wind and water. Locally, the limestone is characterized by greater hardness and ability to withstand physical and chemical weathering than its surrounding environment. Although no rock formations identified as Triassic or Jurassic in age are present in the area, the Pleistocene gravel beds within the Seymour formation are likely made up of materials that originated from formations dating back to the Triassic period. The surface layers of sand and gravel in Haskell and Knox contain a significant quantity of eroded fossils from the Cretaceous period (Nelson et al., 2001; 2013; Winslow & Doyel, 1954).

The geology of the study area is shown in Figure 13. The surface geology consists of Permian-through Quaternary-aged deposits. The Clear Fork and Blair Formations, Permian in age, are the dominant units in the study area. The major lithologic units in the former include mudstone, siltstone, sandstone, dolomite, limestone, and gypsum/evaporite units with a thickness of up to 500 meters (Nelson et al., 2001; 2013; Winslow & Doyel, 1954). Clear Fork unit is the dominant unit in most parts of the study area. The Blair Formations is primarily located in the northwest region of the study area and is composed of interbedded beds of shale, sandstone, gypsum, and dolomite

(The United States Geological Survey (USGS) – Pocket Texas Geology, 2023). Other notable Permian units prevalent in the study area include the Whitehorse Group, the Lueders Formation composed of alternating beds of shale and limestone, the Antlers Sand, and the San Angelo Formation (the northwestern part of the study) which is composed of mudstone, sandstone, siltstone, and gypsum units (Figure 13) (Bureau of Economic Geology (BEG), 2014; USGS – Pocket Texas Geology).

The unconsolidated Quaternary-age sediments are overlying the Permian age deposits and are spatially distributed across almost all parts of the study area (Figure 13). These include the undivided Quaternary deposits (southwestern parts of the study area) associated with alluvium and Pleistocene deposits, and the Seymour Formation (northeastern parts of the study area) that primarily consist of sand and silt and occasionally, gravel units (USGS – Pocket Texas Geology). Another Quaternary units that are prevalent in the study area, though covering small sections/parts (along the central parts of the study area) are the alluvium units. These are mainly floodplain deposits consisting of a mix of silt, clay, sand, fine quartz, and gravel. These deposits were formed on uneven erosional surfaces of the Permian-era red beds, resulting in considerable variation in thickness across the region. The thickness of the alluvial deposits exceeds 100 feet, indicating favorable conditions for groundwater reservoirs (Figure 13). (USGS – Pocket Texas Geology; Winslow et al. 1954).

Several small patches of Cretaceous units are also available in the study area (Figure 13). These include the Edwards Limestone unit, located in the southwestern parts of the study area, which overlies the Comanche Peak Limestone and Walnut formations (Figure 13) (BEG, 2014; USGS – Pocket Texas Geology).

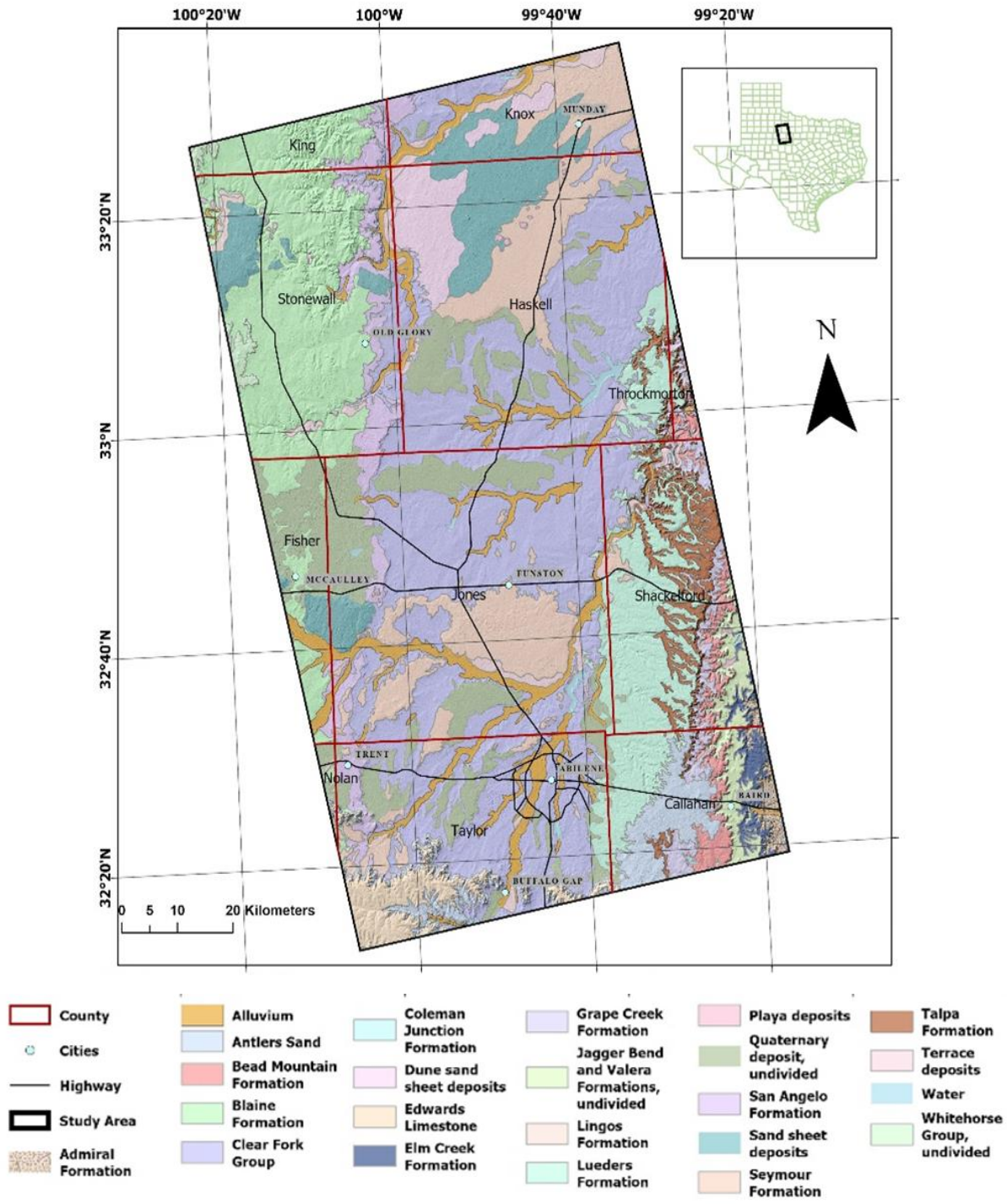

Figure 13:Local geology (USGS – Pocket Texas Geology, 2023)

CHAPTER THREE

DATA AND METHODS

3.1 Overview

Given that most parts of the study area are prone to sinkhole hazards as outlined in section 1.4, minimizing the risk through early detection, monitoring, and characterizing potential sinkholes using cost-effective methods and techniques is of paramount importance. Various multidisciplinary approaches were used in this study to detect, monitor, and characterize the formation of sinkholes across the study area.

Moderate and high-resolution aerial and satellite imagery were among the most essential primary data sources in this research. These images include C-band SAR images obtained from the European Space Agency's Sentinel-1 mission and a 1-m LiDAR DEM of the study area. In addition, other relevant datasets such as multi-temporal groundwater water level data were incorporated into the data analysis. The data processing steps (Figure 14) can broadly be explained through three interconnected procedures. Firstly, depressions that could potentially indicate the presence of active processes resulting from sinkhole activity were identified using methodologies applied to elevation datasets. This was followed by the application of coupled satellite (Synthetic Aperture Radar (SAR)) and ground-based geodetic surface deformation detection techniques to identify depressions experiencing active ground subsidence processes that signify ongoing sinkhole formation processes. The presence of active sinkhole formation processes detected based on the displacement rates, that indicate precursory impending sinkhole formation indicators, derived using the geodetic methods was further validated by mapping the subsurface using near-surface geophysical methods. Finally, processes and factors that induce the formation of sinkholes were determined by integrating various datasets and results including assessing the spatial

relationships of the detected sinkholes and relevant datasets (such as local geology), groundwater wells and their temporal changes in drawdown, etc. Below is a detailed discussion of the datasets and methods used to perform these procedures/tasks.

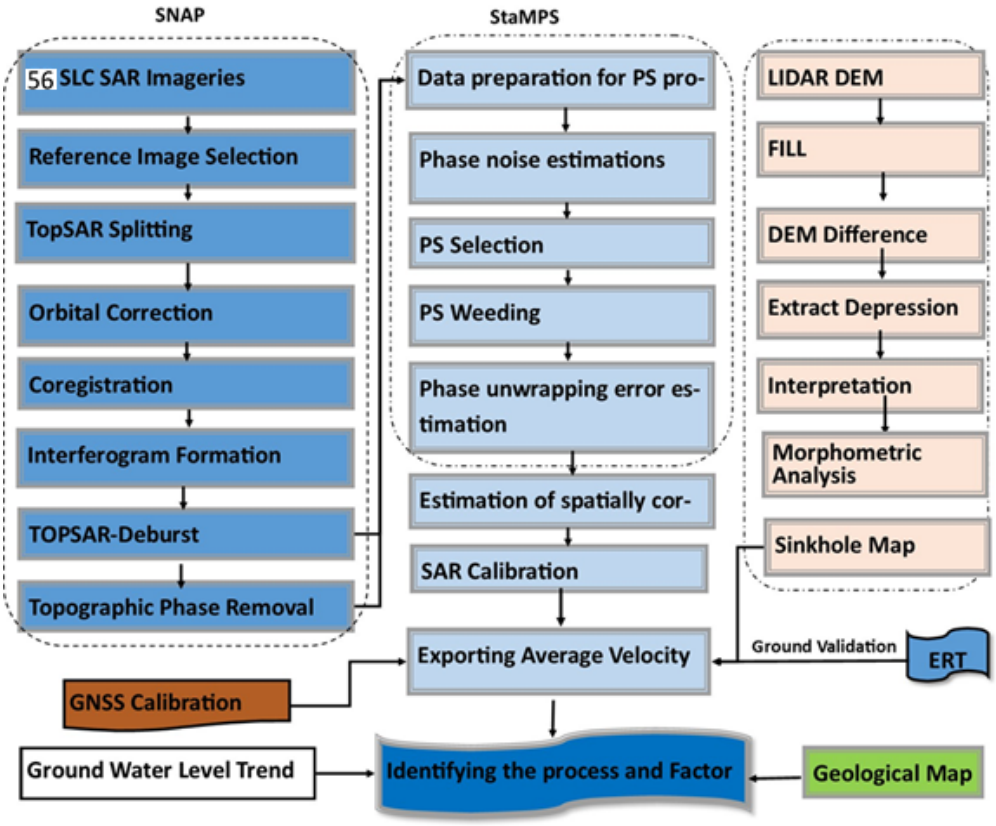

Figure 14: An overview of the deformation estimation, calibration, and validation procedures using the SNAP, StaMPS, and GNSS datasets and methods. Also shown are the relevant datasets that are integrated with the deformation result to further validate the data as well as datasets representing processes and factors that facilitate the formation of sinkholes.

3.2 Mapping Depressions

Sinkholes exhibit specific morphological/physical characteristics compared with the surrounding terrain and these specific characteristics can be used to detect and map their distributions on the earth's surface (de Carvalho Júnior et al., 2013; Shannon et al., 2019). Some of the widely known characteristic traits of sinkholes include their relatively low elevation (depression) and closed shape/morphology (Zhang et al., 2019). Because of this placement of

sinkholes at a relatively lower elevation compared with the surrounding terrain, most sinkhole detection methods exploit the contrast in elevation between the depressions and surrounding landscape to map depressions that could potentially indicate sinkhole activity.

In this study, a high-resolution (1-m spatial resolution) LiDAR Digital Elevation Model (DEM) data was used to extract depressions that could potentially represent sinkhole formations over the study area. The LiDAR elevation dataset was acquired from the Texas Natural Resources Information System (TNRIS) data dissemination platform (https://tnris.org/). The data was provided as compressed LiDAR point cloud data file format (LAZ) that was uncompressed to LAS point cloud data format using tools in ArcGIS software. The LiDAR point cloud data contains hundreds of thousands of first and last return point cloud data with 34 cm spacing between two points. To make it more manageable and for data processing convenience, the LiDAR data were classified into 10,979 different LAS tiles. The size of each tile is around 1200 m by 1200 m and covers roughly 144 hectares. A raster analysis and conversion tool in ArcGIS, called Point Cloud To Raster, was used to convert the point cloud data (LAS file format) to a continuous elevation surface (DEM). The tool used the last returned ground points over the area to generate a 1-m spatial resolution of DEM of the bare earth surface, as a Geotiff layer, using the average Binning technique. This excludes point clouds representing tall features such as buildings and vegetation from the final analysis and the resulting DEM. The binning technique applies interpolation procedures to fill the data gap between the successive elevation points/point cloud data. Once DEMs for each subsection of the study area were generated, they were stitched together (to a single DEM product) using ArcGIS's Mosaic to New Raster tool to produce a DEM representing the entire extent of the study area.

Surface depressions, known as sinks in GIS, are spatially connected cells with undefined flow directions. That is, the flow directions in sinks cannot be assigned to the values of any of the eight surrounding pixel's values as the neighboring cells may be higher or flow into each other (Figure 15) (Zhang et al., 2019). The study used this concept to map all possible sites representing surface depressions.

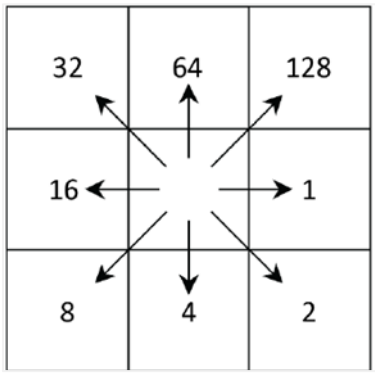

Figure 15: Eight flow directions for all neighboring cells of a focal cell (Zhang et al., 2019).

For mapping the depressions that could potentially indicate sinkhole activity over the study area, the following key procedures were implemented:

- The ArcGIS Fill sink tool within the Hydrology toolset was first used to identify and fill all depressions having lower elevations than the immediate surrounding area (Rajabi et al., 2018) (Figure 16). To identify the location of a depression, the pixels with a comparatively lower elevation than its surrounding pixels were filled to level the area.
- Secondly, the original DEM was subtracted from the filled DEM using the Minus tool in ArcGIS. It subtracted the value of the filled input raster from the value of the original DEM input raster on a cell-by-cell basis (Figure 17). This process omitted all the non-depression surfaces because cells with the same Digital Number (DN) value obtained a zero value, whereas a positive value, which might be a sinkhole depression, was generated when cell

values in the two rasters have contrasting DN values. Values greater than zero are classified as possible sinkhole depression zones using the ArcGIS Reclassify tool and then converted to polygons.

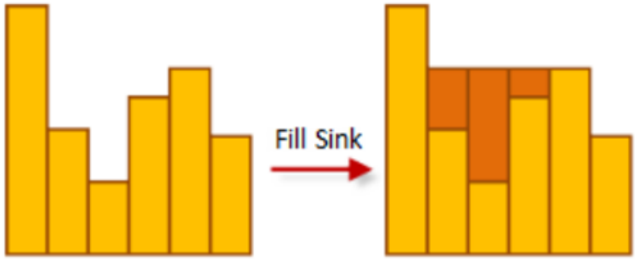

Figure 16: Mechanisms of the fill sink procedure (Environmental Systems Research Institute (ESRI))

Figure 17: Illustration of the process of subtracting DEMs to delineate depressions (ESRI)

- The morphometric characteristics including the size (in terms of area) and shape of the mapped depressions were then analyzed to exclude false alarm features and improve the accuracy of the sinkhole detection procedure. This study aimed to identify moderate- to large-scale sinkholes and hence an area threshold ranging from 600 m^2 to 2600 m^2 was set to retain the depressions whose areas fall within the specified range and discard polygon features outside with areas beyond this specified range. Since sinkholes exhibit circular or near-circular geometric patterns (Subedi et al., 2019), further analysis was undertaken to filter out depressions exhibiting morphometric properties that are not associated with sinkholes. The circularity Index (CI), which takes the area and perimeter of the polygon into consideration,

was used to remove unlikely sinkhole depressions (de Carvalho Júnior et al., 2013; Shannon et al., 2019; Zumpano et al., 2019). The CI value was calculated following equation 2 (Shannon et al., 2019):

$$CI = \frac{\sqrt{4\pi A}}{P} \quad \text{.....Equation 2}$$

where CI is the circularity index, A represents the area, and P represent the perimeter of a polygon.

A circular polygon that is more similar to the geometry of a sinkhole will have a CI value close to 1. Elongated features, in contrast, have a lower value. In a prior study, Shannon et al. (2019) determined that a minimum CI value of 0.85 and a minimum size of 50 ft^2 were applied as thresholds to identify probable sinkholes. In this study, a CI threshold value of 0.86 was used which successfully identified possible circular or elliptical depressions that demonstrated similar physical and morphological characteristics as sinkholes.

Natural and man-made features, such as ponds, lakes, etc., that could potentially be identified/selected as depressions following the above-stated workflow were eliminated from the final product depicting the spatial distribution of potential sinkholes across the study area using spatial hydrology datasets and cross-validating them using high-resolution satellite imagery in Google Earth and land cover data.

3.3 Detecting and validating precursory deformation processes: Quantifying displacements

For detecting active deformation processes that could serve as precursors of ongoing sinkhole activity, 56 Level-1 Interferometric Mode (IW) Sentinel-1 Single Look Complex (SLC) SAR images covering the time interval 2016 – 2021 were downloaded from the Alaska Satellite

Facility Distributed Active Archive Center (ASF DAAC) data archive platform (https://search.asf.alaska.edu/). Seninel-1 mission, currently a constellation of two satellites (Sentinel-1A & Sentinel-1B) equipped with C-band SAR sensors, is operated by the European Space Agency as part of the Copernicus initiative and has a 6–12 data acquisition frequency. The SLC product comprises three sub-swaths each of which is divided into nine bursts (Mandal et al., 2019). Images acquired using the vertical transmit and vertical receive (VV) RADAR polarization mode were used in this study. The total spatial coverage of IW SLC is approximately 150 km and 250 km in the along-track direction and across-track, respectively; while the azimuth and range direction ground resolutions are 20 m and 5 m, respectively (Yagüe-Martínez et al., 2016). The complete list of the SAR imagery used in this study is shown in Table 1.

Table 1: The acquisition dates of the descending track Level-1 IW SLC Sentinel-1 images which were used for quantifying displacement in search of depressions undergoing active displacement in the study area. The image highlighted in the dark gray background is the reference scene.

No.	**Acquisition Date**	**No.**	**Acquisition Date**
1	10/31/2016	**30**	**12/03/2019 (Reference image)**
2	12/18/2016	31	02/01/2020
3	02/16/2017	32	07/21/2019
4	03/24/2017	33	04/13/2020
5	04/05/2017	34	06/12/2020
6	06/16/2017	35	07/30/2020
7	07/10/2017	36	08/11/2020
8	09/08/2017	37	08/23/2020
9	09/20/2017	38	10/10/2010
10	12/13/2017	39	11/03/2020
11	01/30/2018	40	11/15/2020
12	05/06/2018	41	12/09/2020
13	05/30/2018	42	12/21/2020
14	06/11/2018	43	01/14/2020

15	07/17/2018	44	01/26/2021
16	11/02/2018	45	02/07/2021
17	11/14/2018	46	03/03/2021
18	11/26/2018	47	04/08/2021
19	12/20/2018	48	06/19/2021
20	01/25/2019	49	07/25/2021
21	03/14/2019	50	08/06/2021
22	03/26/2019	51	09/11/2021
23	04/19//2019	53	09//23/2021
24	05/13/2019	54	10/05/2021
25	06/06/2019	55	11/22//2021
26	06/18/2029	56	12/28/2021
27	07/21/2019		
28	08/17/2019		
29	11/09/2019		

The displacement rates were calculated using one of the subclasses of the Differential Interferometric Synthetic Aperture Radar (DInSAR) technique (discussed in section 1.3.2.2). The DInSAR technique analyzes the variation in the phase information of two SAR imagery acquired at different times by the same sensor or sensors with similar wavelengths and other properties to determine the change in vertical displacement between acquisition times (Crosetto et al., 2016; 2020). The displacement is estimated by assessing the distinct pattern, called fringes, formed as a result of the interference of the wave information of two phase signals - producing a product called interferogram (Balzter, 2001) (Figure 18). Each fringe represents a phase variation of 2π radians. In addition to the deformation signal, interferograms contain different errors emanating from various sources (equation 3). The goal of the DInSAR technique is to calculate displacement ($\emptyset_{disp}$) by omitting /resolving the other phase components on the deformation signal (Crosetto et al., 2016; Hanssen, 2001; equation 3).

$$\emptyset_{comp} = \emptyset_{disp} + \emptyset_{atm} + \emptyset_{orbit} + \emptyset_{topo} + \emptyset_{noise} \ldots\ldots\ldots\ldots Equation\ 3$$

where $\emptyset_{comp}$ represents the complex interferogram comprising the deformation signal and contributions from other (error) sources, $\emptyset_{atm}$ is the atmospheric phase component, $\emptyset_{orbit}$ represents the contribution due to changes in the satellite's orbit/orbital errors, $\emptyset_{topo}$ is the topographic phase component (also containing the flat-earth phase component), and $\emptyset_{noise}$ is the phase noise.

Though the DInSAR technique can quantify surface displacements up to cm-scale detail, the accuracy is constrained by several factors including temporal and geometric decorrelation that result in poor interferometric coherence, residual atmospheric errors, etc. (Fárová et al., 2019; Pepe & Calò, 2017). Several techniques have been proposed, many of which rely on using sequences of DInSAR interferograms, to mitigate the influences of these errors on the deformation signal to counterbalance the effects of the various sources of residual and decorrelation errors on the displacement estimate (Fárová et al., 2019).

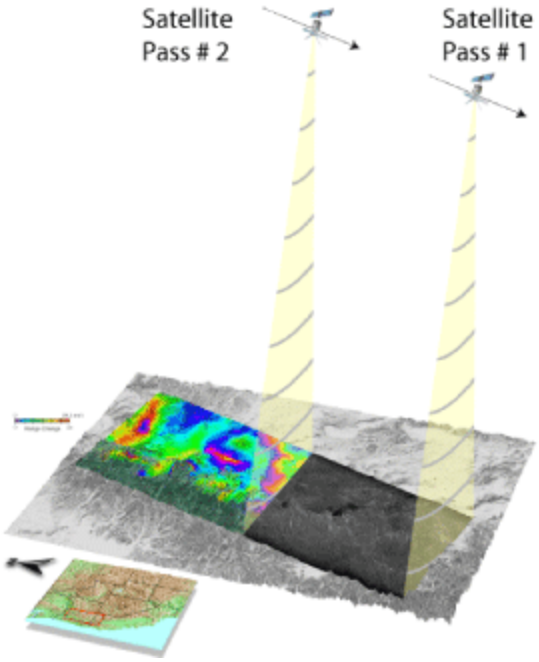

Figure 18: DInSAR method for quantifying displacement (Helz, 2021)

3.3.1 Persistent Scattering Interferometric Synthetic Aperture (PSInSAR)

The PSInSAR method was used in this study to detect active deformation processes and quantify their rates. This method overcomes errors that could limit the accuracy of the conventional InSAR (DInSAR) method, outlined in section 3.3, by analyzing pixels that exhibit phase and scattering stability over a given time, called persistent scatterers (PS), and excluding targets that show poor correlations in the analysis (Hooper et al., 2004; Latip et al., 2019). In the PSInSAR technique, stacks of interferograms generated by cross-multiplying the reference image (primary image) with the complex conjugate of multiple secondary SAR images of the same area are combined to detect and quantify subtle surface deformation velocity of targets that are deemed to be PS targets (Ferretti et al., 2001; Hooper et al., 2004; 2012). The method also compensates for errors and uncertainty, mostly attributed to temporal decorrelation, commonly noted in deformation results obtained by analyzing the cumulative phase of many independent small

scatters, called distributed scatterers (Figure 19), within a resolution cell/pixel (Goel & Adam, 2013; Zhang et al., 2019).

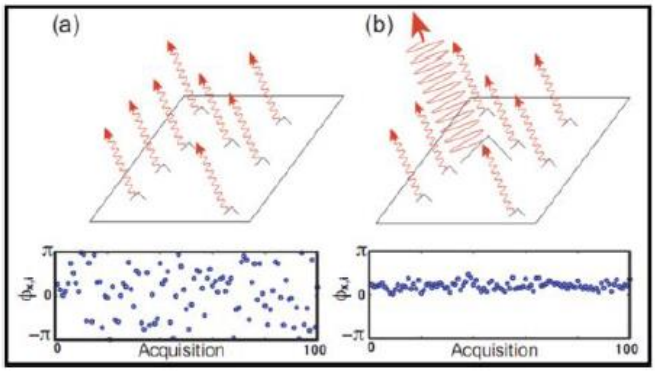

Figure 19: The phase simulation of (a) a distributed scatterer pixel, and (b) a permanent scatterer pixel (Hooper et al., 2007).

In this study, the Stanford Method for Persistent Scatterers (StaMPS) PSInSAR algorithm (Hooper et al. 2004, 2007) was used to identify precursory deformation processes that would indicate ongoing sinkhole formation processes. The 56 Level-1 SLC datasets were initially pre-processed using the Sentinel Application Platform (SNAP) software and integrated into the StaMPS platform to generate the deformation map of the study area. The open-source snap2stamps package consisting of a set of Python-based workflows was used as a bridge to make the SNAP products compatible with the StaMPS processing environment (Alatza et al., 2020; Haley et al., 2022). A schematic diagram demonstrating the workflow highlighting some of the key data processing procedures using the SNAP and StaMPS algorithms is shown in Figure 14. Some of the key pre-processing procedures implemented in the SNAP environment include (Figure 14):

- **Primary Image Selection:** In order to achieve better coherence and high co-registration accuracy, it is essential to select a primary image that is nominally placed with respect to the rest of the images (secondary) in terms of spatial and temporal baseline values (Prats Iraola et al., 2015; Ramirez et al., 2020). The InSAR Stack Overview tool in SNAP, which

automatically selects primary images taking the spatial and temporal information into account, was used in this study. The Sentinel-1 image acquired on December 03, 2019, selected as the primary/reference image using the tool (Table 1).

- **TopSAR Splitting:** In this step, subswaths of the primary image were initially selected/split based on the extent of the study area. This was followed by the splitting of the secondary images. This operation provided the splitting of stitched burst subswath into separate products (Ramirez et al., 2020). In addition, it is important to note that the orbital information provided in the metadata of each SAR image is often inaccurate and needs to be corrected to obtain precise viewing geometry, Therefore, uncorrected orbital information was corrected using accurate orbital information (Yagüe-Martínez et al., 2016). The orbital information correction/update procedure for all the images was applied in this step (Foumelis et al., 2018; Ramirez et al., 2020).
- **Coregistration**: This step involves the geometric aligning of all the images, using the primary/reference image as a base/reference to the rest of the secondary images, followed by the Enhanced Spectral Diversity refinement procedure to achieve fine azimuth coregistration accuracy. Precise orbit information and 3-arcsecond Shuttle Radar Topography Mission (SRTM) DEM were also integrated to further enhance the accuracy of the coregistration step (Tzouvaras et al., 2019).
- **Interferogram Generation:** The coregistered images are then processed to generate an interferogram and interferometric coherence products. The differential interferograms were formed by the difference between the phase values of the two coregistered SAR images and the reference image by using the single-reference interferogram generation method (Cian, 2019). Additionally, the influence of the topography on the deformation signal/interferogram

was removed in this step by simulating the topographic phase using SRTM DEM and subtracting it from the produced interferogram. This was followed by the Debursting procedure in which the subswaths and bursts of the individual interferograms and coherence products were merged to produce spatially continuous products (Foumelis et al., 2018).

- **StaMPS Export:** This step converts the products produced using SNAP algorithms to StaMPS-compatible formats. The exported format contained DEM, diff geo, and rslc files which have essential information for geometric correction and PS candidate selection. This includes elevation data and longitude and latitude information retrieved from the interferograms (Azeriansyah et al., 2019; Foumelis et al., 2018). Once the pre-processing steps were completed and the results were readied for StaMPS integration, the subsequent step involved candidate PS selection within the StaMPS environment. In StaMPS, PS selection is facilitated by taking the PS's amplitude and phase properties into consideration. The amplitude dispersion parameter (D_A), which is the ratio of the standard deviation of the temporal amplitude and mean values (Equation 4), was initially used to identify potential PS pixels with strong reflectivity.

$$D_A = \frac{\sigma_A}{\sigma_A}, \quad \text{Equation 4}$$

Where D_A represents amplitude dispersion parameter while σ_A and σ_B signify the standard deviation and mean amplitude values, respectively (Ferretti et al., 2001; Hooper et al., 2007).

Except for few major settlements and urban centers, the study area largely comprises agricultural or barren landscapes (Figure 10). As a result, a higher amplitude dispersion value (0.42) was used so that the PS candidate selection would include scatterers and produce a high density of PS candidates outside the urban centers. Following the selection of the PS candidate

pixels, the subsequent processing steps for producing the complete deformation field of the study area proceeded using a series of Matlab scripts described as follows (Figure 14):

- **Phase Noise, Temporal Coherence Estimation, and PS Selection:** In this step, the spatially correlated and uncorrelated phase noise values for each candidate pixel in the interferogram were estimated and refined in a series of iterations. The temporal coherence value for each one of the PS candidates, selected based on the amplitude dispersion coefficient, was then estimated using residual phase values derived from the series of interferograms created using the SNAP algorithm. A coherence threshold value of 0.3 was set to isolate and retain pixels that demonstrate phase stability and exclude candidates that exhibit high amplitude dispersion but low temporal coherence (Palanisamy Vadivel et al., 2019).
- **PS wedding:** This procedure eliminates some of the previously selected PS candidates. These include duplicated PS candidates, which were due to error geocoding, and PS candidates due to signal contribution from neighboring pixels were dropped from candidates of PS. Then noisy phases with a standard deviation value greater than one were removed (Kesaraju, 2012).
- **Phase correction and unwrapping:** To recover the original phase change due to actual deformation, the spatially uncorrelated look angle (DEM) errors that were calculated earlier were removed from the wrapped phase at this stage. This was followed by the phase unwrapping procedure aimed at resolving the ambiguity problem of the wrapped phase of the PS pixels $(-\pi,+\pi]$ using the Statistical Cost Network Flow Algorithm for Phase Unwrapping (SNAPHU) algorithm. The phase unwrapping restored the correct multiple of 2π to each PS point to obtain quantitative interpretation. Finally, spatial filtering was applied to estimate and remove any spatially correlated errors from the deformation estimate (Ab Latip & Aobpaet,

2018; Reigber and Moreira, 1997; Costantini, 1998; Palanisamy Vadivel et al., 2019; Werner et al., 2002).

- **Displacement rate estimation:** The unwrapped phase observations were then used to estimate the mean line of sight (LOS) displacement rates given in millimeters per year (mm/yr) units. Positive displacement rates indicate the motion of the PS pixels towards the satellite (uplift) while negative values signify the motion of the PS away from the satellite (subsidence).
- **Atmospheric correction:** The contribution of the tropospheric (atmospheric) phase on the final deformation estimate was modeled and removed using the Toolbox for Reducing Atmospheric InSAR Noise (TRAIN) (Bekaert et al., 2015). The data was finally exported to a GIS-compatible file type for subsequent analysis and interpretation.

3.3.2 PSInSAR Displacement Rate Validation: Global Navigation Satellite System (GNSS) Data

As outlined in sub-section 3.3.1, the PSInSAR technique is a useful method for measuring land surface displacement over time. Though the majority of the various potential sources of errors that could affect the accuracy and reliability of the deformation estimate obtained using the PSInSAR method were modeled and removed as outlined above, the presence of residual errors could degrade the quality and accuracy of the deformation estimate. As a result, displacement estimates are commonly calibrated using displacement rates of ground-based permanent GNSS stations calculated using a satellite-based geodetic technique (Gili et al., 2000). This method uses a satellite-based permanent GNSS constellation system to continuously provide positioning, navigation, and timing (PNT) services on a global or regional basis. The long-term (2006 – 2023) mean annual displacement rate estimated at the TXAB permanent GNSS station (Figure 10) was used in this study to calibrate the deformation

rate calculated using the PSInSAR method. The dataset was acquired from the online data dissemination platform of the Nevada Geodetic Laboratory (http://geodesy.unr.edu/).

3.4 Sinkhole Detection Model Validation: Electrical Resistivity Tomography

The robustness of the sinkhole detection approach which was largely based on remote sensing datasets and analysis techniques applied to the datasets was validated through ground-based techniques capable of mapping and characterizing the subsurface in search of features and morphological attributes that are associated with sinkholes. The 2D ERT survey, that combines vertical electrical sounding (VES) for determining the physical property of the surface with depth and the horizontal profiling (HP) for assessing the lateral and vertical changes of the subsurface in contrast to the surrounding rock and soil units (Hussain et al., 2020b; Nart COŞKUN, 2012), was chosen in this study for this purpose. The 2D ERT survey (Figure 20) was conducted using the SYSCAL R1 plus instrument in an area (Figure 21) that exhibited high land subsidence rates and whose concentric morphology resembled sinkhole features. The basic principle behind detecting sinkhole features using this technique is that when a known amount of direct electrical current is injected in and flows in the subsurface and changes of potential difference between two electrodes are recorded, it can be used to calculate the electrical resistivity of materials within the subsurface that depends on the material's response to the passage of current. This property, in turn, is used to detect and map potential sinkholes (Hussain et al., 2020; Loke et al., 2013). The presence of water/saturated soil or bedrock/cavity will create conditions for high conductivity of the electrical current with little resistance and hence will exhibit a relatively low resistivity value. On the other hand, air-filled caves or air-filled pore spaces will have high resistivity values. Hence, it can be concluded that both saturated on unsaturated sinkhole features with low resistivity subsurface or high resistivity can be detected by the ERT method (Kidanu et al., 2020; Muhammad et al., 2012;

Zhou et al., 2002). The procedures followed in this study for mapping the subsurface using the ERT method are summarized below:

- First, a field survey site located near the intersection between Grape and Franklin Road in North Abilene town (Figure 21) was selected. This area was identified because it fulfilled the two conditions set in this study for identifying potential sinkhole sites (section 3.2) – that the area contained features that resemble (geometric and morphologic aspects) features associated with sinkholes, derived using the depression delineation technique outlined in section 3.2, and the area is experiencing active high subsidence rate (<= -3.5 mm/yr) that was estimated using the fused PSInSAR and GNSS techniques (section 3.3).
- Defining the electrode spacing for the ERT survey is very important because it determines the penetration depth and ability to observe vertical and lateral changes within the subsurface. In general, a bigger/wider electrode spacing is preferred for a deeper investigation but at the expense of reduced lateral resolution. On the other hand, the lateral resolution is improved with a smaller electrode spacing (Montgomery et al., 2020). Because the present study is aimed at understanding the characteristics of the dissolution processes near the surface, a moderate electrode spacing configuration that can capture the lateral and vertical changes in the electrical property of the subsurface with a moderate resolution was selected. As a result, the Wenner array configuration with a total of 24 electrodes arranged with a spacing of 5 meters (Figure 8; Figure 20) was used to map the subsurface layers with moderate resolution. The Electre Pro software was used to create/program sequences of measurements that were uploaded to the SYSCAL Pro R1 for automated field data acquisition. A maximum depth of investigation of 18.2 m was attained based on the settings applied to the Electre Pro software.

Figure 20: Geophysical (ERT) survey using the Wenner array.

- After data acquisition, the data was transferred (downloaded) to the Prosys II software for filtering erroneous or redundant measurements. The data was exported to a format compatible with the data inversion software – the Res2DINV (Loke and Barker, 1996). The inversion step produced a 2D resistivity model of the subsurface depicting the lateral and vertical changes of electrical resistivity.

Figure 21: ERT survey (A–B) area near a refilled sinkhole site. The depression was extracted using LiDAR data (marked as black polygon), and the nearby PS point (marked as red point) revealed a displacement rate of -3.5 mm/yr.

3.4 Understanding the controlling factor

Excessive and uncontrolled withdrawal of groundwater resources creates severe environmental implications such as aquifer depletion and groundwater and soil contamination. Moreover, it may induce land subsidence processes that, in combination with other factors and processes, may result in severe natural disasters with adverse repercussions for humans, the economy, and the environment (Babaee et al., 2020; Parvin et al., 2019). As indicated in section 1.2, subsidence in the form of brittle and ductile sagging occurs when excessive pumping rates and the subsequent lowering of the groundwater remove the buoyant support provided by the

groundwater to the overburden. This will increase the effective stress and eventually could form sinkholes (Kim et al., 2019). Many researchers have reported the link between declining of groundwater levels, land subsidence, and sinkhole formation (Baer et al., 2018; Khanlari et al., 2012).

Hence, this study used current and historical groundwater level datasets to understand the mechanism of the sinkhole formation processes taking groundwater pumping-induced land subsidence into consideration. This factor was considered because of the prevalence of large-scale agricultural activities that undertake excessive pumping of groundwater (Figure 12) which led to significant groundwater declines (Bruun et al., 2016). The deformation patterns of the PS points that exhibited subsidence and fall within the areas identified as potential sinkholes based on their geometrical and morphological characteristics in conjunction with the local geology were compared against historical and current groundwater levels of wells that are proximal (within 500 m) to the PS points. The current and historical groundwater level datasets (1956 – 2021) were downloaded from the Texas Water Department Board (TWDB) database. The groundwater levels were plotted against time (timeseries) showing the multitemporal groundwater level fluctuations over time. The timeseries graph of the ground displacement was superimposed on the groundwater level change graph in search of a relationship that could be used to establish the causative processes and factors that form sinkholes in the area. This relationship was also used to forecast the possibility of sinkhole processes over parts of the study area where there were enough datasets demonstrating excessive groundwater withdrawals resulting in significant declines in the groundwater tables over areas with geometric and morphometric properties similar to sinkholes, but there were few or no PS pixels nearby the areas depicting displacement due to lack of interferometric coherence and other factors. The reverse conditions, where there are PS pixels

within closed depressions undergoing gradual subsidence but there were no publicly-available groundwater or relevant datasets, were also considered (in conjunction with other datasets) to indirectly infer the processes that gave rise to the formation of the sinkholes.

To offset the inconsistency in terms of data gaps, variable time coverage, etc. of the publicly-available multitemporal groundwater level data, this study used the groundwater well density map/product (Figure 22) to map the current groundwater wells density/distribution in a given area, which could potentially give an indication of the level of groundwater use in an area. This approach is widely used in sinkhole susceptibility mapping. For instance, Ozdemir (2015) used groundwater well density map to identify areas that are prone to sinkholes in the Karapinar district in Turkey.

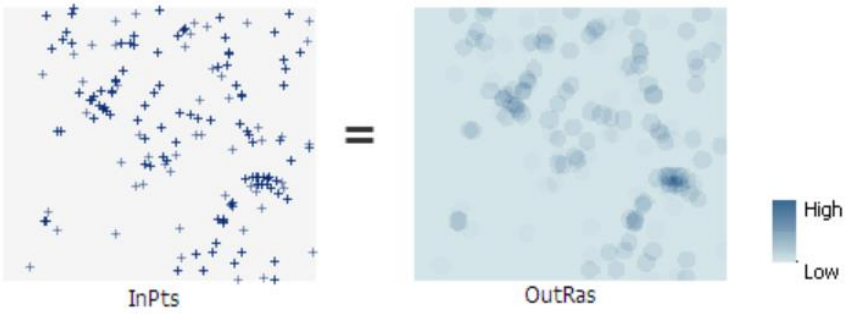

Figure 22: Illustrations of density map formation from point datasets (ESRI)

The density map technique converts points (in this case, wells) to estimate and generate a surface density map that summarizes the distribution and clustering of the points (wells) by assigning more weights to nearby points (wells) than those farther away and then summing up all the weighted points (wells) within the predefined kernel size (Hu et al., 2018). The ArcGIS Kernel Density tool within the Spatial Analyst Tools was used to generate the groundwater well density map which was then classified into low, medium, and high density based on the number of wells per km^2.

CHAPTER FOUR

RESULTS AND DISCUSSION

4.1 Overview

In this chapter, a detailed description of the outcomes generated by analyzing the individual or combination of datasets using the techniques described in chapter three is provided. A comprehensive overview of the interpretation of the results and the interrelationship among the various analysis results is also presented.

4.2 Depression delineation

The methodology depicted in the flowchart described in Figure 14 was applied on the LiDAR datasets to identify the depression zones in the study area. In the method, prospective sinkholes were generated by the difference between the original and filled DEM, and pixels whose values were greater than 0 were identified as depressions that could represent potential sinkhole morphology. The technique yielded a total of 538,394 depression features whose areas range from 9 m^2 to 5000 m^2 (Figure 23). A manual classification technique was used to classify and display (as a graph) based on their sizes (area) for further analysis and interpretations (Figure 23). The result indicated that the majority (88%) (Figure 24) of the identified depressions are less than 300 m^2 in area, followed by the depressions with 300 – 600 m^2 areal extent (Figure 23). On the other hand, depression polygons with areal extents greater than 2600 m^2 (1%) were also obtained using the analysis. These were deemed to represent potential errors emanating from inherent errors in the data, false detections, or geometries representing other features (Figure 24). Several studies stated that most sinkhole features within the Rolling Plain typically have diameters ranging from less than 30 m (more than 700 m^2 area) to as high as 100 m (more than 7800 m^2) (Caran &

Baumgardner, 1990; Martinez et al., 1998). Hence, only polygons with areas within the range of 600 m^2 to 2600 m^2 (Figure 25) were selected for further analysis.

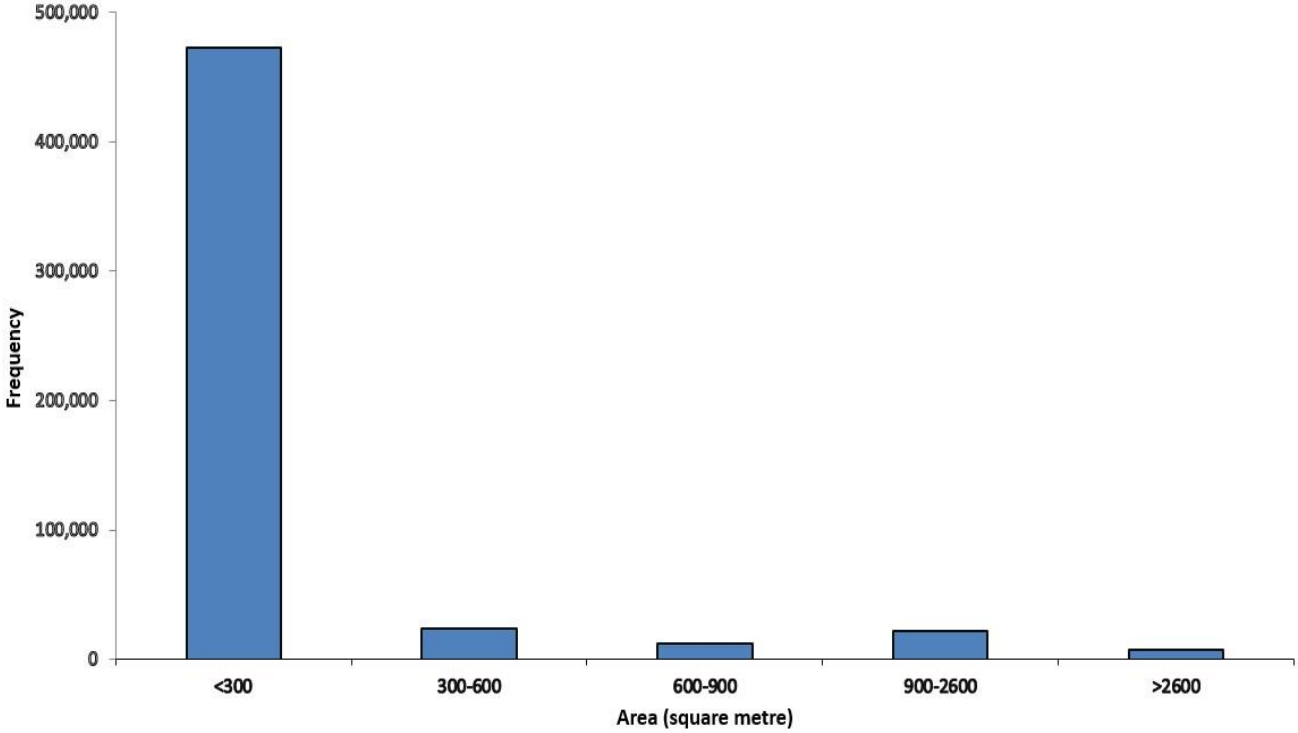

Figure 23: Six groups of total area surface depression (given in m^2). Polygons/depressions with areas less than 600 m^2 and greater than 2600 m^2 were removed and the remaining were retained for further investigation.

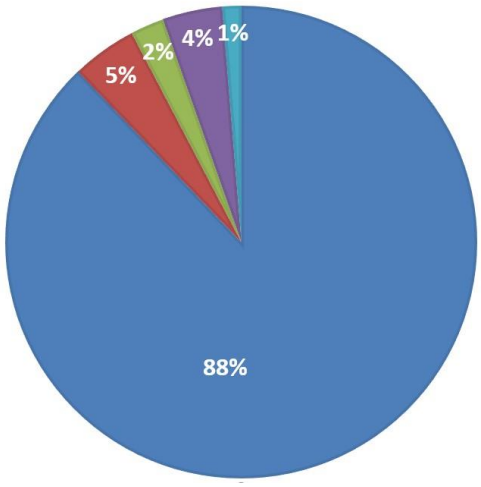

Figure 24: Percentage of depression based on their size/area (polygons with areas of <300 m^2 (88%), >2600 m^2 (1%) and (300-600 m^2) (5%) were removed while those with 600-900 m^2 (2%) and 900-2600 m^2 (4%) areas were retained for further investigation).

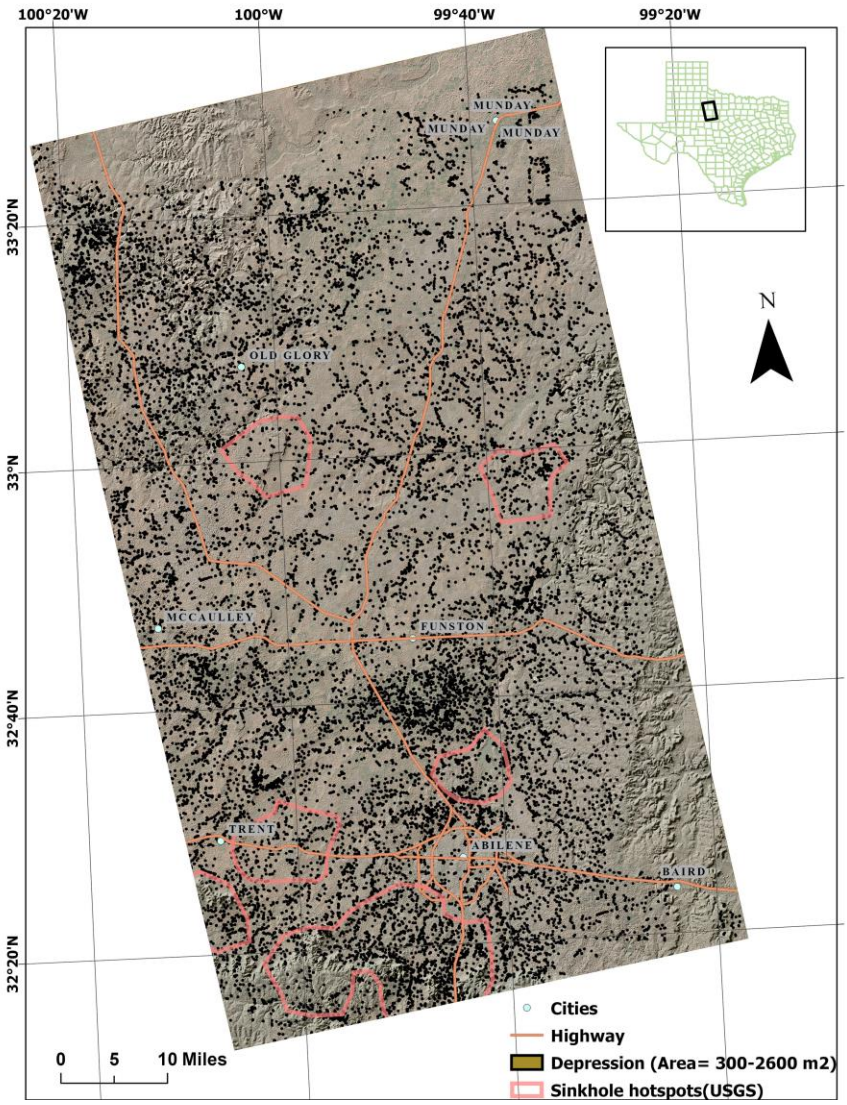

Figure 25: Spatial distribution of depressions with areas between 600 to 2600 m^2. The depressions on the map exhibited circular and elongated shapes, but due to the map's small scale, the size and details of these depression features were not clearly visible.

The CI analysis (Figure 26), whose inherent values range from 0 to 1, was then applied to the remaining polygons to identify depressions that demonstrate sinkhole-like morphology (near-circular to circular) and filter out non-circular/irregular-shaped depressions that represent other processes or features, or residual false detections. Most of the features in the study area have CI values ranging from 0 to 0.8. Close inspection of the features revealed that most of these features with these values represent either hydrological features (streams, rivers) based on the hydrological

data obtained from the Texas Water Development Board (TWDB) (http://www.twdb.texas.gov/) or man-made features (construction works, etc.) (Figure 26). As a result, a CI threshold value of 0.86 was used to filter only features with circular or near-circular morphological attributes that potentially represent sinkhole or sinkhole-like depressions. This eliminated most of the features that were initially retained based on their geometry from the final result (Figure 27).

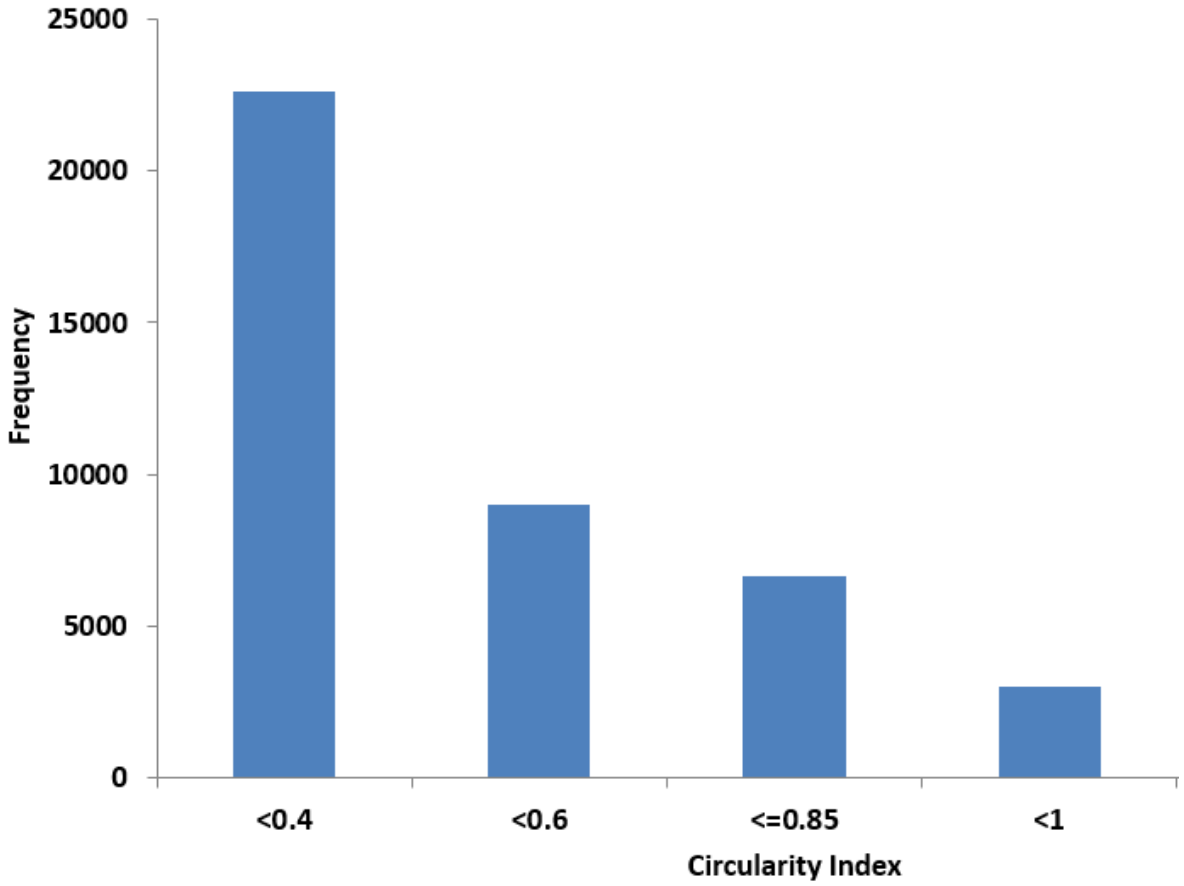

Figure 26: Four groups of cumulative circularity index values derived after applying of geomorphometric analysis. A threshold value of 0.85 was used to retain circular or near circular features.

The final result obtained based on the set CI cutoff value was further examined for potential inaccurate detections and rectified by overlaying the result with land use and land cover, hydrological network data, and other ancillary data resources (such as Google Earth). Though LiDAR sensors can acquire elevation data of the surface (bare ground) beneath canopy covers and hence can be used for successfully detecting sinkholes in such settings (Kobal et al., 2015), the

absence of limited last returns particularly in dense canopy covers can limit the reliability of the data and the depression mapping. ESRI's land cover data (10-m spatial resolution (https://livingatlas.arcgis.com/landcover/) which is derived from multi-temporal Sentinel-2 datasets (Venter et al., 2022) complements this drawback of the LiDAR-based depression/sinkhole detection procedure by verifying the accuracy of the LiDAR-derived spatial distribution of sinkholes located underneath dense canopy covers as well as detect sinkhole features based on the land cover patterns. Wu et al. (2016) used land use/land cover data to supplement the results of sinkhole mapping in Filmore County (Minnesota) using LiDAR data. They observed that most of the sinkholes in the county were spatially concentrated on flat hilltop areas proximal to river valleys which are dominated by agricultural crops and grassland/herbaceous land cover types (Wu et al., 2016).

Each of the context data, sources, and parameters that were assessed and used for refining the result, as described above, are summarized in Table 2. This process further significantly reduced the number of depressions by 21% that were retained based on their CI cutoff value (Figure 27).

Table 2: Context elements and their parameters.

Context Data	Sources	Parameter were used
Circular/Near circular manmade Infrastructure	Google Earth Image	Falsely detected sinkholes were removed, such as stadiums, construction excavations, etc.
Land Use/Land Cover	ESRI Land Cover 10m	To complement/validate sinkhole detections in areas with dense canopy covers.
Hydrology	From Texas Water Department	Objects that are falsely identified as sinkholes were removed such as ponds.

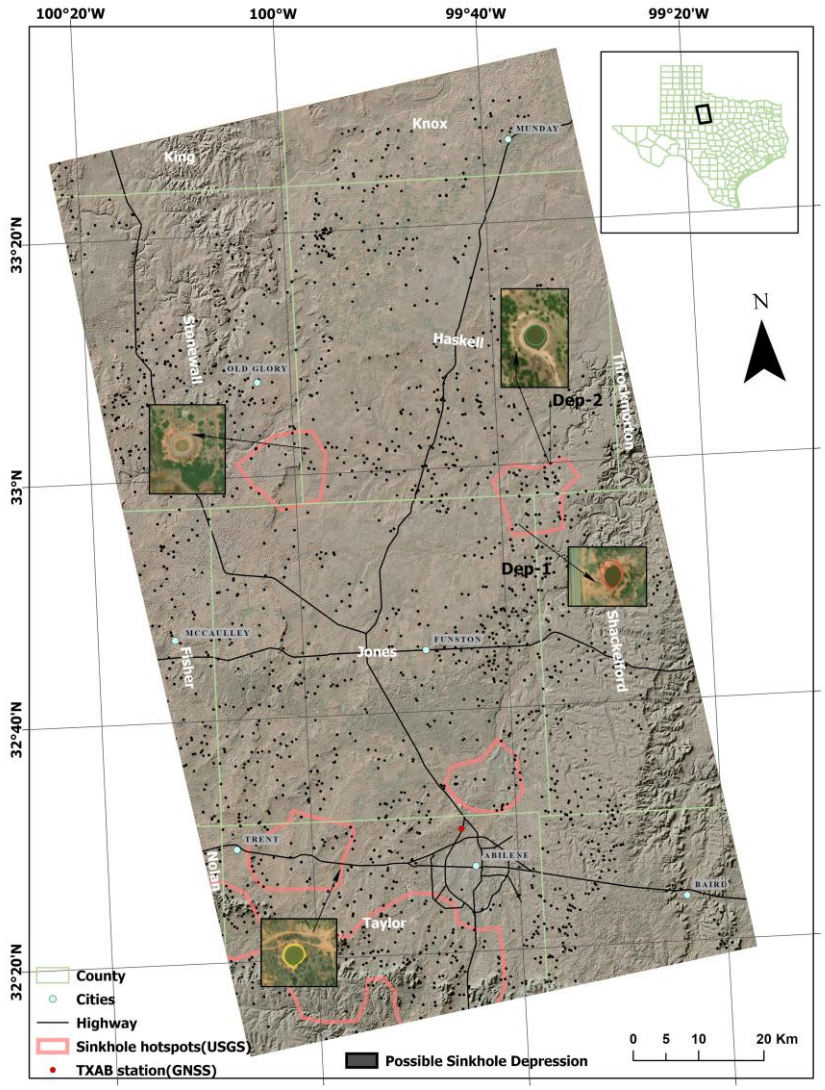

Figure 27: The spatial distribution of potential sinkholes in the study area derived using LiDAR datasets and calibrated/validated using other relevant datasets and techniques (Table 2). Also shown on the map are the sinkhole hotspots mapped by the USGS (pink), major cities, highways, and the TXAB GNSS station.

The final result of the analysis procedure for mapping potential sinkholes outlined above, using depressions as a proxy, is shown in Figure 27. The result revealed a network of depressions, ranging in size from 600 m^2 to 2600 m^2 and with a CI value of 0.86, spatially distributed almost across the entire extent of the study area. The result also showed that many small depressions are spatially clustered in northeast, west, central, southcentral (near Abilene), and southeastern areas

(Figure 27). Some of these depression clusters detected in this study lie within the sinkhole hotspot identified by the USGS (shown in pink color in Figure 27). A closer examination of some of the depressions using a Google Earth satellite image showed that some of the depressions mapped in this study as potential sinkholes were indeed sinkholes. For example, several depressions including those shown as Dep-1 and Dep-2 (Figure 27) were identified as potential sinkholes based on the methods and results discussed above. The Google Earth image of the area supported the assessment derived in this study indicating that the spatial distribution of several sinkholes in the analyzed areas overlaps with the depressions mapped in the study (Figure 27).

One of the primary objectives of the present study was to identify depressions that could potentially transition to sinkholes and incur damage to humans and property. Hence, it is imperative that actively deforming depressions are identified using other approaches as the potential sinkhole mapping exercise using the LiDAR data is incapable of detecting active ground displacement. The PSInSAR method was used for such purpose to detect depressions undergoing active displacement that could eventually form sinkholes.

4.3 Surface deformation

Displacement rates (in mm/yr) across the study area were calculated by the PSInSAR technique using the Sentinel-1 SAR data acquired from 2016 to 2021. This would be crucial in identifying active displacement rates that could over time induce sinkholes, and identifying contributing factors that exacerbate the development of the features. The resulting deformation result was validated by comparing the vertical displacement component of the permanent GNSS station (TXAB), located north of Abilene (Figures 10 and 28), which was acquired from the Nevada Geodetic Laboratory and the nearest PSInSAR pixel

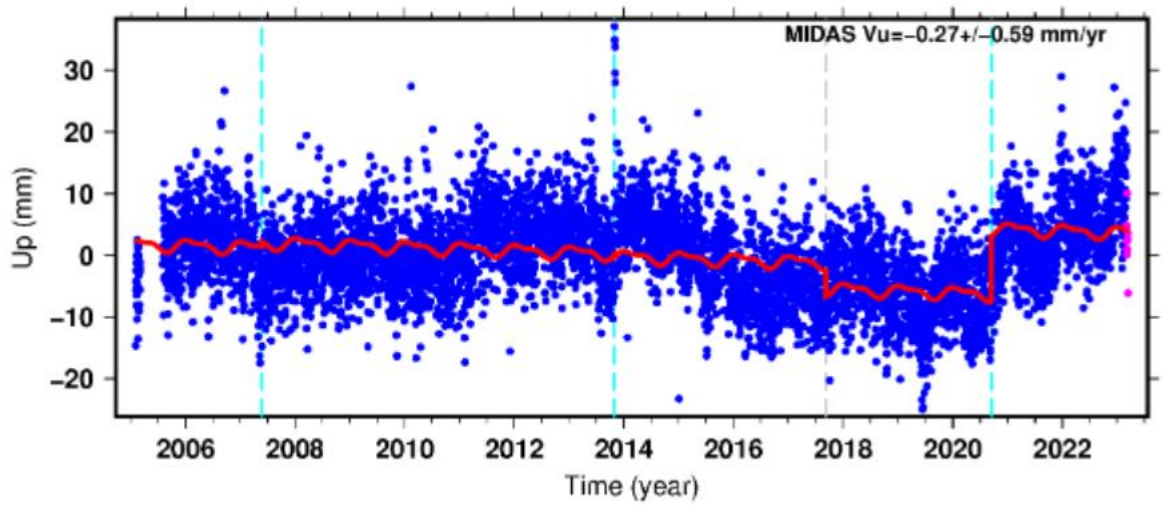

Figure 28: TXAB station daily positional data graph from 2006 – present.

The surface deformation rates derived using the approach outlined above are shown in Figures 29, 30, and 31. The result showed that the ground deformation rate across the study area ranges from 7.15 to -6.15 mm/yr where negative values indicate subsidence in which the target moves away from the satellite while positive values indicate uplift indicating the target is moving towards the satellite. A mean deformation (2006 – 2022) deformation rate of -0.27+/-0.59 mm/yr was calculated at the TXAB station (Figure 28) which was compared with the displacement rate of the nearest PS point (Figure 31) located nearly 20 m away from the GNSS station to determine the accuracy of the displacement estimation using the PSInSAR method. The displacement rate calculated at the PS pixel indicated a displacement rate of -0.56 mm/year which falls with the error margin of the GNSS displacement results. This suggests that the results of the PSinSAR displacement analysis were sufficiently reliable for the purposes of this study.

The mean of the overall displacement rate in the study area was calculated to be 0.003 mm/yr (standard deviation: 1.3) signifying that there was little to no displacement in the majority parts of the study area during the investigated interval (Figure 29). However, patches of land (shown as light black color in Figure 31) particularly in central, northern, western, southern, and

southeastern parts of the study area display significant subsidence rates (mean: -3.04 mm/yr) (Figure 30). This suggests that substantial geological processes are occurring in these areas that are causing the ground to relatively move more rapidly than in the surrounding stable area.

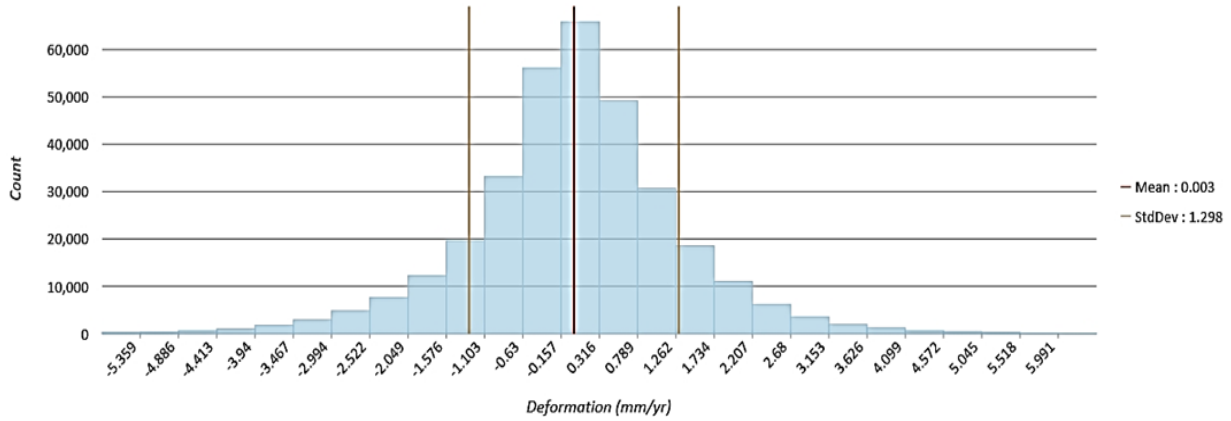

Figure 29*:* A histogram demonstrating the frequency and rate of deformation (mm/yr) in the study area. The mean value of the deformation rate is 0.003 mm/yr (near stable deformation) with a standard deviation 1.3.

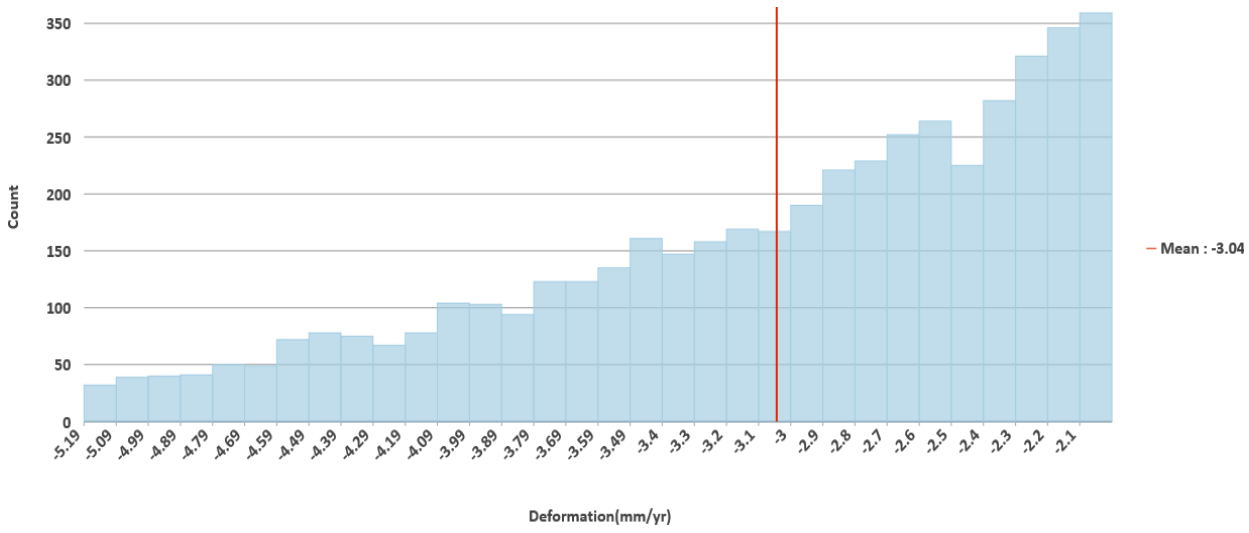

Figure 30: Deformation rates (mm/yr) of selected subsidence zones (potential sinkholes) (shown in light black outline in Figure 31).

Fourteen subsidence zones were selected across the extent of the study area (shown by black-outlined polygons in Figure 31) as potential sinkhole sites due to the higher subsidence rate. These anomalous areas were identified by observing a spatial clustering of PS points with mean

subsidence values ranging from -2 to -5.19 mm/yr (Figure 31). The selected subsidence zones were compared with the sinkhole hotspot previously identified by the USGS (Figure 31, shown in light blue dashed outline) for potential spatial correspondence/overlap among the selected subsidence zones.

The overall deformation characteristics in these selected zones were demonstrated by the temporal deformation patterns observed at PS points contained within the identified subsidence zones. Two persistent scatterers points, namely a' and b' located within the subsidence zones of TS-1 and TS-3 (Figure 31), respectively, which are undergoing active deformation, were examined to assess the pattern and temporal change in the deformation characteristics of the depressions (Figure 31). For the subsidence zone of TS-1, the subsidence rate detected at the PS location a' was -4 mm/yr. The deformation pattern at the PS point (a') shows a steep declining trend (Figure 32) indicating the active ground deformation processes that may or may not be associated with the formation of sinkholes. In the case of the PS point 'b' located in the subsidence zone of TS-3, the temporal deformation rates vary from -2.03 to a relatively higher subsidence rate of -5.19 mm/yr and exhibit a subsiding deformation pattern (Figure 32). Several studies forecasted the occurrence of sinkholes by identifying such precursory and consistently incremental subsidence deformation patterns (Baer et al., 2018; Talib et al., 2022).

The highest displacement rates among the subsidence zones were observed at the PS points located within the sites TS-1 (and the patches of land to the north (Knox County) and west (Stonewall County) of it (Figure 31)), TS-2 (and the area located at the boundary of Fisher and Stonewall counties (Figure 31)), TS-3 (and the area to the west of TS-3 (Figure 31)), TS-4, and TS-5 spatially located at the southcentral, west, north and northeastern parts of the study area (Figure 31). The detected subsidence rates in these areas range from -2.1 to -5.18 mm/yr, with an

average rate of -3.11(Figure 31). The highest subsidence rates (-5.19 mm/yr) were recorded in PS pixels located within TS-1 and TS-3. The former and zones associated with it do not spatially overlap with the sinkhole hot spot zones mapped by the USGS while the latter subsidence zone, located near Abilene City, completely falls within the hotspot. Similar spatial correspondences were noted for the subsidence zones southwest of Abilene, and near Trent City (east of TS-3) both of which are located in Taylor County, and (partially) at TS-2 (Figure 31). These areas are presumed to be at risk of sinkhole hazards.

Other sites in the study area that exhibited moderate subsidence rates and whose distribution partially or completely overlaps with the dense networks of depressions, and some with the USGS sinkhole hotspots, were also considered as sites where there is a high probability of sinkhole activity. For example, sites TS-A and TS-B area in the southwest and southeastern parts of the study area, where the mean subsidence rate at the two sites is -2 and -2.2 mm/yr, respectively, are potential sinkhole sites. Despite not being located in the sinkhole USGS hotspot zone, this study uncovered a significant downward motion near Bairo City at the TS-A zone (Figure 31) which is believed to be due to sinkhole activity. On the other hand, portions of the southern and southwestern areas along the gorge were found to undergoing moderate to higher subsidence rates in this study partly fall within the sinkhole hotspot zone mapped by the USGS. These zones are underlain by units belonging to the Clear Fork Group and the Blain Formation (Figures 13 and 31). Similarly, several PS points exhibiting moderate rates of subsidence rates (up -3.3 mm/yr) that are assumed in this study to be areas of high sinkhole hazard are spatially clustered along the rivers in the northeast and west regions of Old Glory City located within the subsidence zone TS-5 and around border area between Haskell and Knox counties (Figure 31). Likewise, the two subsidence zones located to the northeast and northwest of Abilene (TS-4 and TS-6) also

demonstrate moderate (to high) rates of subsidence. This irregular pattern of deformation corresponds with the reported characteristics of sinkholes and the spatial extent of the processes that induce their incidence – that sinkhole formation in most cases is an isolated/localized incident driven by local processes (Intrieri et al., 2018).

.

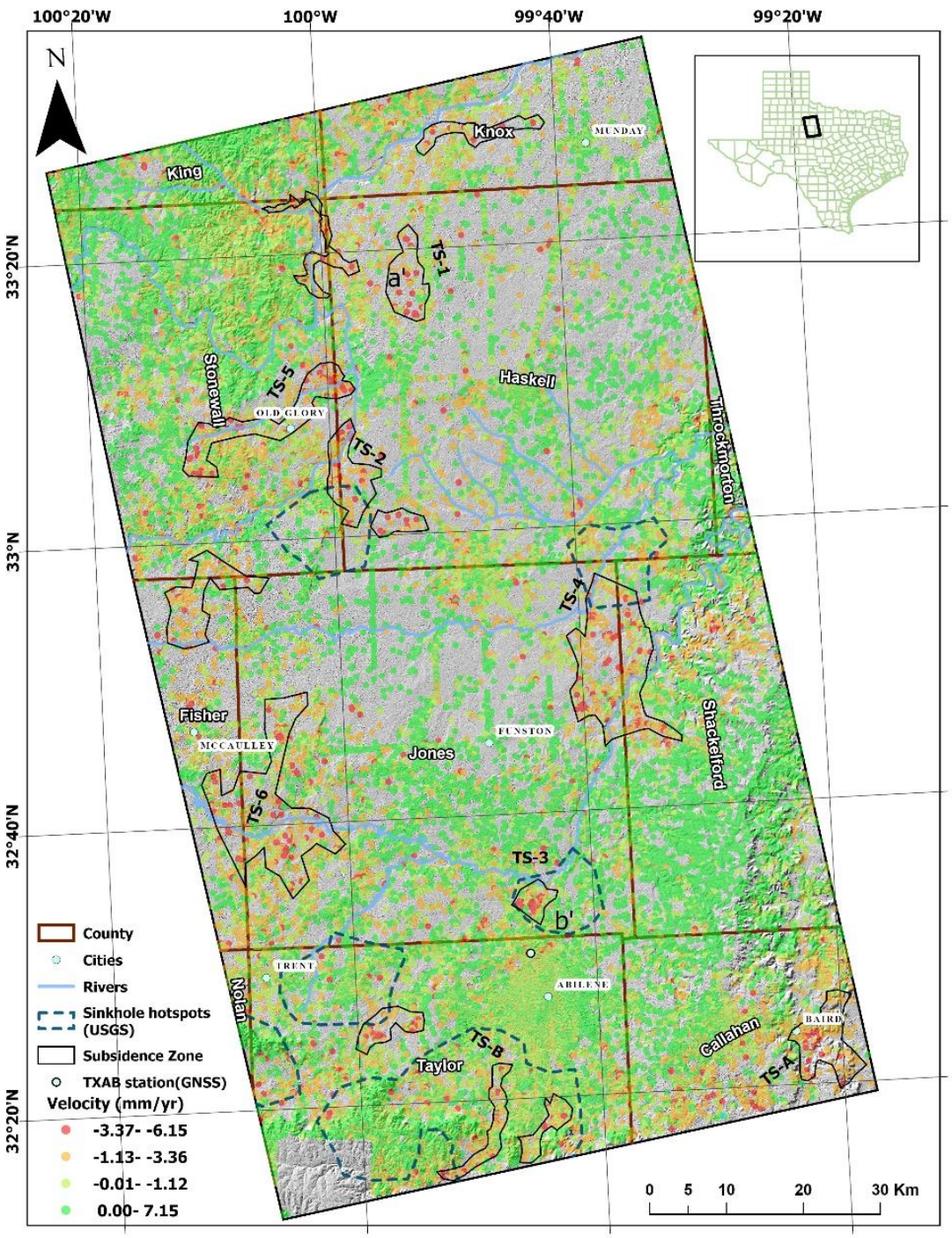

Figure 31: Deformation velocity map (mm/yr) calculated using the PSInSAR method applied on Sentinel-1 SAR data (2016 – 2021). Selected zones where sinkholes potentially could form (delineated based on their rates of subsidence and the presence of depressions derived using LiDAR data) are shown in black-outlined polygon. Sinkhole hotspots in the stud area which were delineated by the USGS in earlier studies are also shown (dashed blue color).

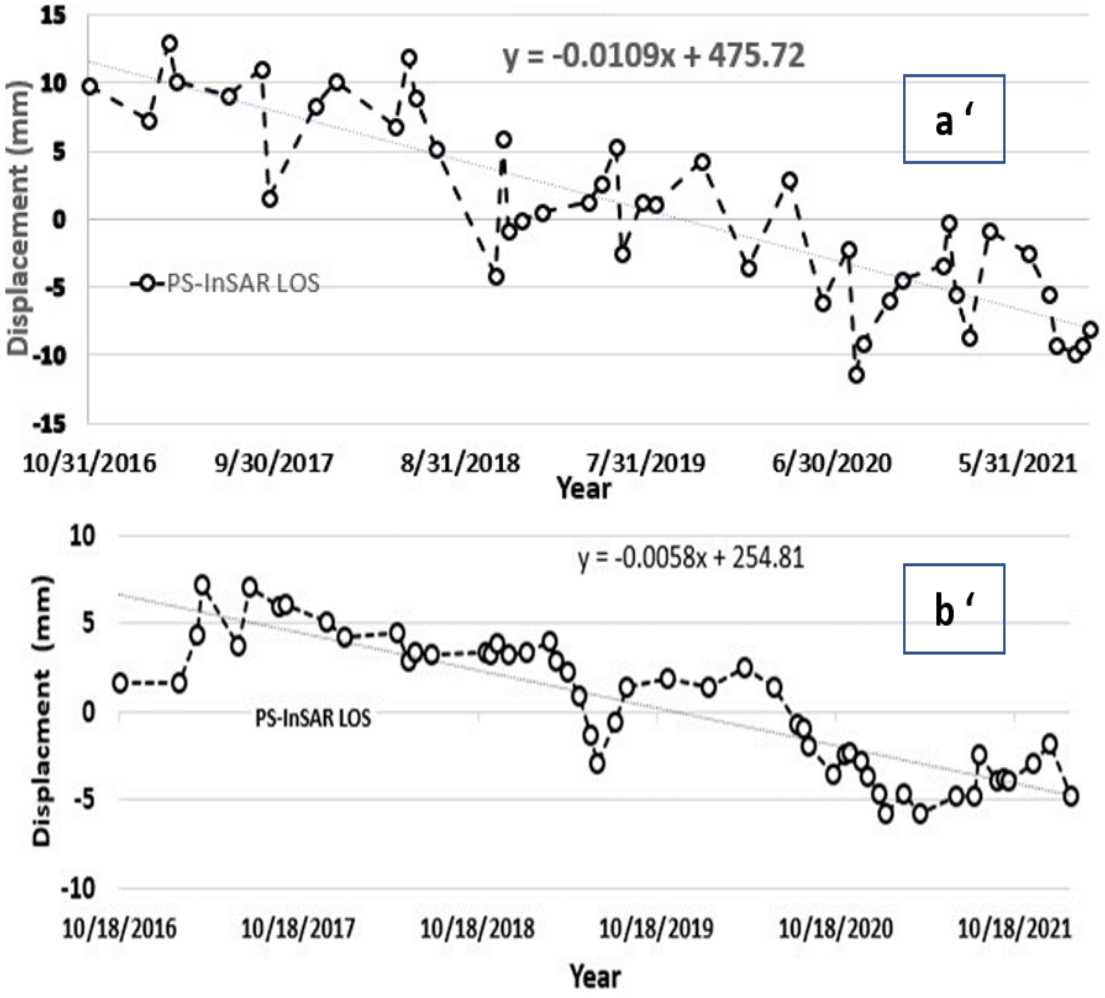

Figure 32: LOS displacement PSInSAR a' and b' over time at subsidence TS-1 and TS-3 subsidence zones, respectively (see Figure 31 for the location of the PS points).

4.4 Electrical Resistivity Tomography

Though the deformation estimates obtained using the PSInSAR analysis in conjunction with the GNSS data were able to detect actively moving (subsiding) depressions that can be used as a proxy for mapping sinkholes, the reliability of the result should be validated using other methods. This is because of the fact that final PSInSAR results could still contain residual errors that will introduce errors and uncertainties in the deformation estimate. Hence the ERT method was employed in this study to map/observe the subsurface to obtain crucial information that could potentially indicate the presence of void or water-saturated cavities that through time and given

favorable conditions could translate into sinkholes. An east-west oriented ERT survey was conducted in an area located north of Abilene City in Taylor County (Figure 21) – an area where a high subsidence rate (-3.5 mm/yr) from the PSInSAR was observed and is proximal to a site where a sinkhole incident was reported in recent years. The 2D resistivity profile obtained from the survey (Figure 33) illustrates variations in electrical resistivity both laterally and vertically, and the findings are discussed in the following sections.

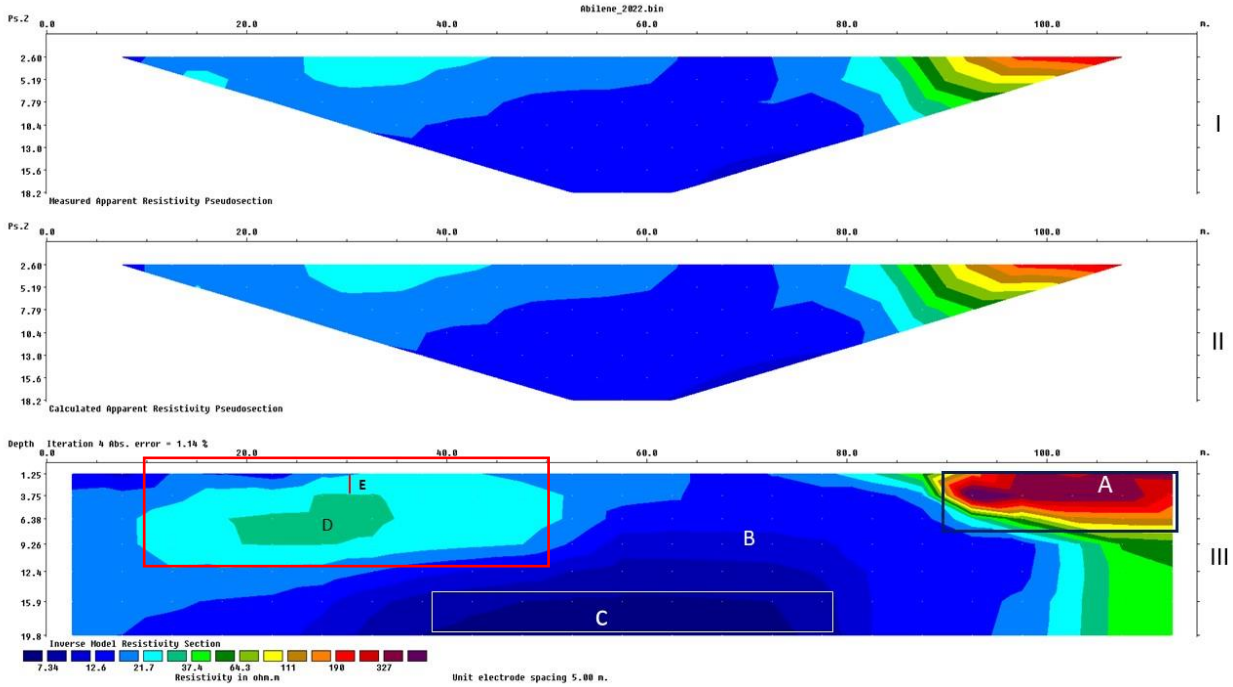

Figure 33: 2D ERT result demonstrating the lateral and vertical change of electrical resistivity and the RMSE error. The anomaly shown in red-outlined circle is a potential sinkhole interpreted in this study.

Figure 33 shows the inverted 2D electrical resistivity profile of the investigated area (Figure 33(III)). A high resistivity layer labeled as A was found at a depth of up to 5.5 meters on the east side. This layer was interpreted as bedrock (as it has resistivity values ranging from 150 to 327 ohm-m (Montgomery et al., 2020)). A low resistivity layer (B) was detected at an approximate depth range of 1.25 m to 19 m. This layer was found to stretch to both the West and East of the

high conductivity region (marked as C) and was interpreted as a saturated clay layer (marked as B (Figure 33(III)) (Pazzi et al. 2018). The higher conductivity was obtained at the lower part of the profile (marked as C) which may contain a solution filled with clay. As shown in Figure 33 (marked D), there is a large anomaly (approximately 16 m long laterally) that exhibited relatively low resistivity (high conductivity) with values ranging from 30 to 37 ohm-m (depth ~5 m). In contrast with the resistivity of the surrounding area, site D's resistivity is relatively indicating a potential sinkhole being present at this site. The resistivity difference between this particular site and its surrounding area is substantial (up to 30 ohm-m). This area is considered a possible void (cavity) created by the dissolution of the Clear Fork Group of soluble rocks and could potentially result in the formation of a sinkhole by causing the overlaying clay layer to sag/subside downward (towards the cavity) and eventually collapsing into the cavity/void.

4.5 Formation Mechanism and Controlling Factors

As discussed in section 1.2, the presence of soluble rocks has a higher contribution to the formation of sinkholes. Due to the prevalence of evaporate rocks in the study area (Figure 13), several sinkholes have formed and as a result, have adversely impacted property and resources. In the following section, the processes and factors that induce ground deformation and over time lead to the formation of sinkholes will be discussed.

As outlined above, the area lying in Knox County and proximal to the county boundary (with Haskell County) (located northwest of TS-1 and shown by a black-outlined polygon), contains a number of depressions undergoing moderate to high subsidence rates (Figure 31). Most of the depressions are adjacent to the nearby river (Figure 31). Similarly, a number of PS points within the TS-4 (located northeast of Abilene) and the TS-2 subsidence zone (located at the boundary between Haskell and Stonewall Counties) which are proximal to the nearby waterbodies also exhibited moderate to high subsidence rates (up to -5.13 mm/yr) (Figure 31). The majority of

these PS pixels are located in an area that is overlain by the Clear Fork Group which contains soluble materials such as Limestone, Dolomite, and Gypsum (Figure 13). It's hypothesized in this study that percolation of water through fractures and joints and their interaction with the Clear Fork Group units are dissolving the soluble units, causing cavity and subsidence, and potentially facilitating the formation of sinkholes (Figure 31). Similar association between moderate to high subsidence rates and proximity to waterbodies were also noted for the TS-5 area (Figure 31). The Blain Formation, also characterized by the presence of soluble units such as gypsum which are interbedded with dolomite, is the dominant unit in this part of the study area (TS-5). Memon et al. (1999) noted the influence of seeps from springs and surface waterbodies in facilitating the formation of cavities and sinkholes within the Blaine Formation in the north-central parts of the rolling plains physiographic region of Texas.

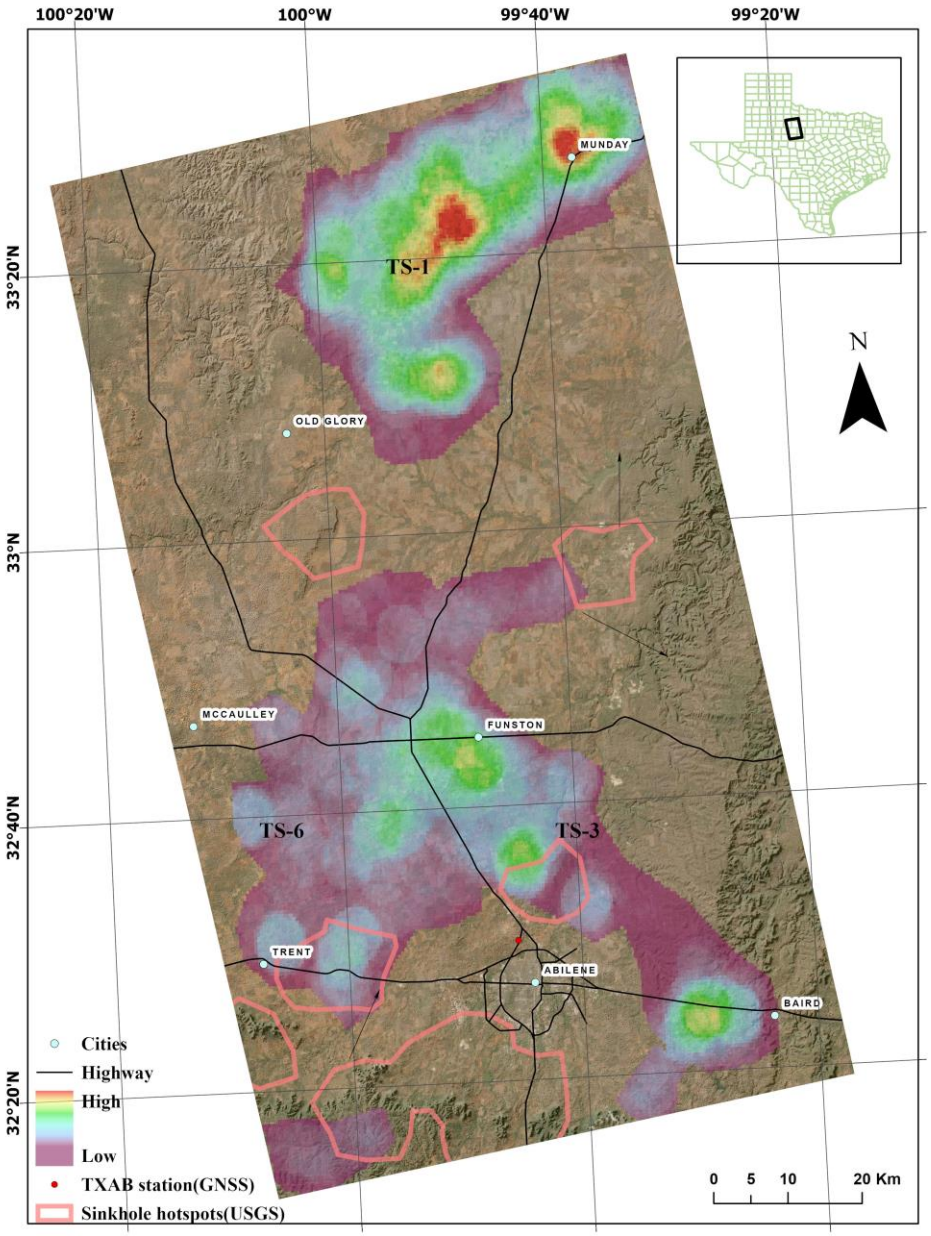

Figure 34: Groundwater density map. Red color represents high number of wells clustered together, and magenta color represents sparsely distributed wells.

As discussed in Chapter 1, groundwater is one of the main resources used for several purposes in the study area – particularly for agriculture. The groundwater density map shown in Figure 34 was derived by analyzing the spatial distribution and clustering of groundwater wells across the study area. The high well density corresponds with areas known for their agricultural activities where groundwater is intensively used for irrigated farming. There is also a high spatial

correlation between the high well density areas and some of the subsidence zones that exhibited moderate to high subsidence rates such as TS-1 and TS-3 (Figure 34). For instance, the TS-3 zone is known for its extensive agricultural activity, and the local communities rely on groundwater pumping from the SA as a primary water source. The long-term (1998 – 2022) groundwater level records of a well located within the TS-3, an indirect indicator of pumping rates, show that the groundwater level has declined significantly over time (Figure 35). Though the temporal span of observation is not similar as the groundwater records, the deformation pattern of the PS pixel closest to the well (subsidence rate at b' PS point) demonstrates a similar trend (Figure 35).

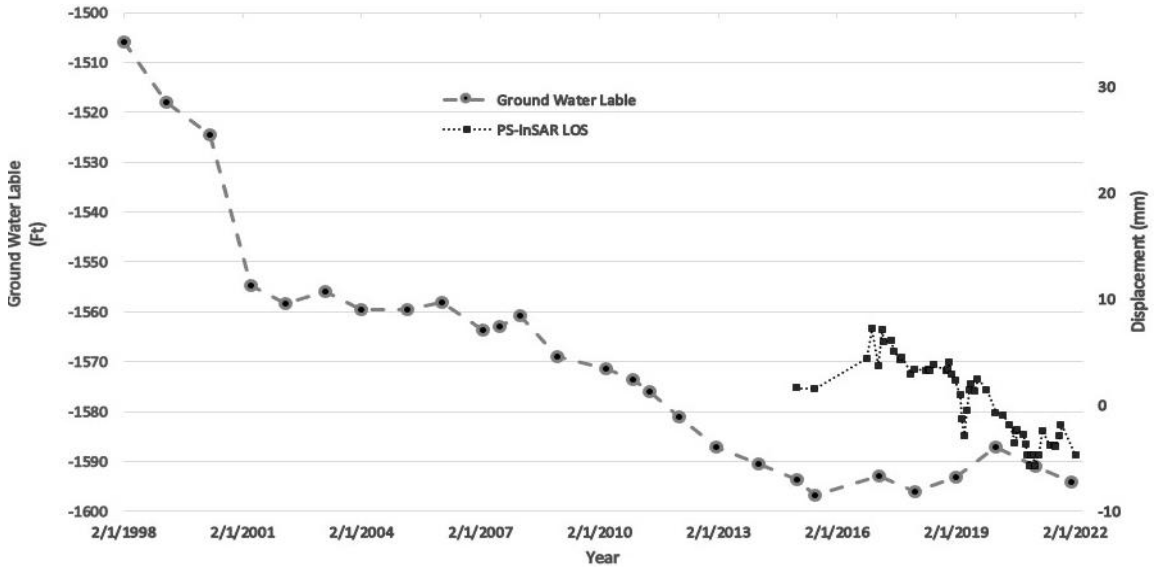

Figure 35: Groundwater pumping and PSInSAR pattern (at PS point b') at TS-3 subsidence zone (see Figure 31 for the location of the PS points).

Figure 35 provides clear evidence of excessive exploitation of groundwater in the study area. As demonstrated by the well data (Figure 35), the groundwater table in the TS-3 area has been lowering since 1998. The interaction of groundwater with the soluble units belonging to the Clear Fork group in this area has potentially resulted in the formation of cavities and the gradual lowering of the water table removes the buoyant support provided by the groundwater to the overlying units leading to the progressive sagging of the overburden (subsidence) and potentially

could form sinkholes. Hence, the PSInSAR shown in Figure 35 could be used as a precursor for an impending sinkhole formation in the TS-3 zone. The USGS assessment of the area, as sinkhole prone, also supports the assessment put forward in this study (Figure 35).

The risk of sinkhole incidence is slightly different in the case of the TS-1. As noted in section 2.3, substantial areas in the northeast of the study region are encompassed by the SA, which is comprised of unconsolidated materials such as coarse sand and fine silt of dune sand sheet and sand sheet deposits geological formation (Figure 12). This also includes the TS-1 subsidence zone which is also dominated by the SA. In the TS-1 and surrounding zones, groundwater pumped from the SA is being used for irrigation and other activities. The higher pumping rates have caused groundwater decline and subsequently resulted in subsidence induced by the loss of pore pressure and compaction. Figure 36 demonstrates a similar trend that is exhibited by the groundwater levels and surface deformation rates. But, contrary to the TS-3, a sinkhole is not expected to be formed in this area as the settings conducive for the formation of sinkholes are lacking. This particularly entails the absence of soluble carbonate or evaporite units.

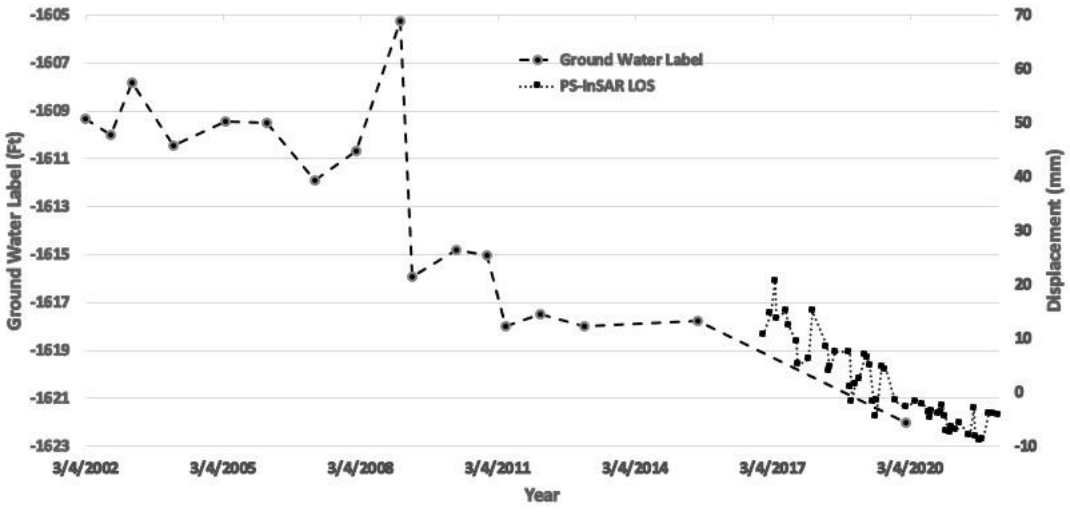

Figure 36: Groundwater pumping and PSInSAR pattern (at PS point a') at TS-1 subsidence zone ((see Figure 31 for the location of the PS points).

CHAPTER FIVE

CONCLUSION

This study applied an integrated approach including multisource remote sensing datasets and ground-based observations to detect potential sinkhole features and map their spatial distributions by assessing the geometric and geomorphic properties of the surface features and their long-term displacement patterns. Moreover, the study identified natural and anthropogenic-led processes and factors that induce the formation of sinkholes.

The potential sinkhole sites were initially identified by mapping depressions using high-resolution LiDAR data. A geometric and morphologic assessment, coupled with the validation of the results using ancillary data, was undertaken to delineate depressions that could potentially be sites of sinkhole activity. The PSInSAR method was then employed to detect depressions undergoing subsidence to identify active sinkhole processes that could over time form sinkholes. The result indicated that substantial areas of the project site which are overlain by the evaporite and carbonite units belonging to the Clear Fork Group and Blain Formation are undergoing subsidence that could result in catastrophic hazards associated with sinkholes. It was also found that excessive groundwater pumping and the subsequent decline in the groundwater levels are the leading causes that induced the formation of the sinkholes.

One of the key limitations of this research was the lack of sufficient stable or persistent scatterers to quantify the displacement in various parts of the study area. This was mainly because of the fact that the study area is predominantly agricultural fields that caused frequent changes in land use and land management practices leading to a decline in interferometric coherence. Furthermore, the medium resolution provided by the Sentinel-1 data made it challenging to

identify and track small-scale sinkhole features. The limited number of ERT surveys, due to the lack of access to many of the potential sinkhole sites, could also partly constrain the accuracy of the findings.

REFERENCE

Alatza, S., Papoutsis, I., Paradissis, D., Kontoes, C., & Papadopoulos, G. A. (2020). Multi-temporal inSAR analysis for monitoring ground deformation in Amorgos Island, Greece. *Sensors (Switzerland)*, *20*(2).

Al-Kouri, O., Al-Fugara, A., Al-Rawashdeh, S., Sadoun, B., Sadoun, B., & Pradhan, B. (2013). Geospatial Modeling for Sinkholes Hazard Map Based on GIS & RS Data. Journal of Geographic Information System, 05(06).

Aley, T. J., Williams, J. H., & Massello, J. W. (1972). Groundwater contamination and sinkhole collapse induced by leaky impoundments in soluble rock terrain.

Ali, H., & Choi, J. H. (2019). A review of underground pipeline leakage and sinkhole monitoring methods based on wireless sensor networking. In *Sustainability (Switzerland)* (Vol. 11, Issue 15).

Argentieri, A., Carluccio, R., Cecchini, F., Chiappini, M., Ciotoli, G., de Ritis, R., di Filippo, M., di Nezza, M., Marchetti, M., Margottini, S., Materni, V., Meloni, F., Nardi, A., Rotella, G., Sapia, V., & Venuti, A. (2015). Early stage sinkhole formation in the Acque Albule basin of central Italy from geophysical and geochemical observations. In *Engineering Geology* (Vol. 191).

Alrowaimi M, HB Yun, Chopra M (2015) Sinkhole physical models to simulate and investigate sinkhole collapses, in Doctor DH, Land L, Stephenson JB (eds): *14th Sinkhole Conference NCKRI Symposium* 5, 559–568.

Ashworth, J. B., & Hopkings, J. (1995). Aquifers of Texas. *Texas Water Development Board Report 345*, *380*(July).

Aydan, O., & Ito, T. (2015). The effect of the depth and groundwater on the formation of sinkholes or ground subsidence associated with abandoned room and pillar lignite mines under static and dynamic conditions. *Proceedings of the International Association of Hydrological Sciences*, *372*.

Azeriansyah, R., Prasetyo, Y., & Yuwono, B. D. (2019). Land Subsidence Monitoring in Semarang and Demak Coastal Areas 2016-2017 Using Persistent Scatterer Interferometric Synthetic Aperture Radar. *IOP Conference Series: Earth and Environmental Science*, *313*(1).

Babaee, S., Mousavi, Z., Masoumi, Z., Malekshah, A. H., Roostaei, M., & Aflaki, M. (2020). Land subsidence from interferometric SAR and groundwater patterns in the Qazvin plain, Iran. *International Journal of Remote Sensing*, *41*(12).

Baer, G., Magen, Y., Nof, R. N., Raz, E., Lyakhovsky, V., & Shalev, E. (2018). InSAR Measurements and Viscoelastic Modeling of Sinkhole Precursory Subsidence: Implications for Sinkhole Formation, Early Warning, and Sediment Properties. *Journal of Geophysical Research: Earth Surface*, *123*(4).

Balzter, H. (2001). Forest mapping and monitoring with interferometric synthetic aperture radar (InSAR). *Progress in Physical Geography*, *25*(2).

Basso, A., Bruno, E., Parise, M., & Pepe, M. (2013). Morphometric analysis of sinkholes in a karst coastal area of southern Apulia (Italy). *Environmental Earth Sciences*, *70*(6).

BEG, 2014. Annual Report. [accessed 2022 July 5]. https://store.beg.utexas.edu/annual-reports/2202-ar2014.html.

Benito, G., del Campo, P. P., Gutiérrez-Elorza, M., & Sancho, C. (1995). Natural and human-induced sinkholes in gypsum terrain and associated environmental problems in NE Spain. *Environmental Geology*, *25*(3).

Bekaert, D. P. S., Walters, R. J., Wright, T. J., Hooper, A. J., & Parker, D. J. (2015). Statistical comparison of InSAR tropospheric correction techniques. *Remote Sensing of Environment*, 170, 40-47.

Benito-Calvo, A., Gutiérrez, F., Martínez-Fernández, A., Carbonel, D., Karampaglidis, T., Desir, G., Sevil, J., Guerrero, J., Fabregat, I., & García-Arnay, Á. (2018). 4D monitoring of active sinkholes with a Terrestrial Laser Scanner (TLS): A Case study in the evaporite karst of the Ebro Valley, NE Spain. *Remote Sensing*, *10*(4).

Blasco, J. M. D., Foumelis, M., Stewart, C., & Hooper, A. (2019). Measuring urban subsidence in the Rome Metropolitan Area (Italy) with Sentinel-1 SNAP-StaMPS Persistent Scatterer Interferometry. *Remote Sensing*, *11*(2).

Bobrowsky, P. T., & Brian Marker. (2017). Encyclopedia of Engineering Geology. *Encyclopedia of Engineering Geology*, *August 2019*.

Bruun, B., Jackson, K., Lake, P., & Walker, J. (2016). Texas Aquifers Study Groundwater Quantity, Quality, Flow, and Contributions to Surface Water.

Caran, S. C., & Baumgardner, R. W. (1990). Quaternary stratigraphy and paleoenvironments of the Texas Rolling Plains. *Bulletin of the Geological Society of America*, *102*(6).

Carbonel, D., Rodríguez, V., Gutiérrez, F., Mccalpin, J. P., Linares, R., Roqué, C., Zarroca, M., Guerrero, J., & Sasowsky, I. (2014). Evaluation of trenching, ground penetrating radar (GPR) and electrical resistivity tomography (ERT) for sinkhole characterization. *Earth Surface Processes and Landforms*, *39*(2).

Chai, J. C., Shen, S. L., Zhu, H. H., & Zhang, X. L. (2004). Land subsidence due to groundwater drawdown in Shanghai. *Geotechnique*, *54*(2).

Chaudhuri, S., & Ale, S. (2014). Temporal evolution of depth-stratified groundwater salinity in municipal wells in the major aquifers in Texas, USA. *Science of the Total Environment*, *472*.

Chen, H., Oguchi, T., & Wu, P. (2018). Morphometric analysis of sinkholes using a semi-automatic approach in Zhijin County, China. *Arabian Journal of Geosciences*, *11*(15).

Closson, D., Karaki, N. A., Klinger, Y., & Hussein, M. J. (2005). Subsidence and sinkhole hazard assessment in the Southern Dead Sea area, Jordan. *Pure and Applied Geophysics*, *162*(2).

Corradetti, A., Seers, T., Mercuri, M., Calligaris, C., Busetti, A., & Zini, L. (2022). Benchmarking different SfM-MVS photogrammetric and iOS LiDAR acquisition methods for the digital preservation of a short-lived excavation: a case study from an area of sinkhole related subsidence. *Remote Sensing*, 14(20), 5187.

Crosetto, M., Monserrat, O., Cuevas-González, M., Devanthéry, N., & Crippa, B. (2016). Persistent Scatterer Interferometry: A review. In *ISPRS Journal of Photogrammetry and Remote Sensing* (Vol. 115).

Crosetto, M., Solari, L., Mróz, M., Balasis-Levinsen, J., Casagli, N., Frei, M., Oyen, A., Moldestad, D. A., Bateson, L., Guerrieri, L., Comerci, V., & Andersen, H. S. (2020). The evolution of wide-area DInSAR: From regional and national services to the European ground motion service. In *Remote Sensing* (Vol. 12, Issue 12).

Cueto, M., Olona, J., Fernández-Viejo, G., Pando, L., & López-Fernández, C. (2018). Karst-induced sinkhole detection using an integrated geophysical survey: A case study along the Riyadh Metro Line 3 (Saudi Arabia). In Near Surface Geophysics (Vol. 16, Issue 3).

Dailey, H. J. (2020). Characterization of Surface Karst Using LiDAR and Field Traverses, Fort Hood Military Installation, Coryell County, Texas.

de Carvalho Júnior, O. A., Guimarães, R. F., Montgomery, D. R., Gillespie, A. R., Gomes, R. A. T., Martins, É. de S., & Silva, N. C. (2013). Karst depression detection using ASTER, ALOS/PRISM and SRTM-derived digital elevation models in the Bambuí group, Brazil. *Remote Sensing*, *6*(1).

Deb, D., & Choi, S. O. (2006). Analysis of sinkhole occurrences over abandoned mines using fuzzy reasoning: A case study. *Geotechnical and Geological Engineering*, *24*(5).

Doctor, D., & Young, J. (2017). *An Evaluation of Automated GIS Tools for Delineating Karst Sinkholes and Closed Depressions from 1-Meter LiDAR-Derived Digital Elevation Data*.

Drees, L. R. (1986). SOIL CHARACTERISTICS AND GENESIS OF CARBONATES IN THE ROLLING PLAINS OF TEXAS (MICROMORPHOLOGY, EOLIAN DUST, STABLE CARBON ISOTOPE). Texas A&M University.

Emil, M. K., Sultan, M., Alakhras, K., Sataer, G., Gozi, S., Al-Marri, M., & Gebremichael, E. (2021). countrywide monitoring of ground deformation using insar time series: A case study from Qatar. *Remote Sensing*, *13*(4).

Engelbrecht, J., Inggs, M. R., & Makusha, G. (2011). Detection and monitoring of surface subsidence associated with mining activities in the Witbank Coalfields, South Africa, using differential radar interferometry. *South African Journal of Geology*, *114*(1).

English, S., Heo, J., & Won, J. (2020). Investigation of sinkhole formation with human influence: A case study fromwink sink in Winkler county, Texas. *Sustainability (Switzerland)*, *12*(9).

ESA. (2018). *Sentinel-1 SAR User Guide Introduction*. Sentinel Online.

Environmental Systems Research Institute (ESRI). (2023). GIS Mapping Software, Location Intelligence & Spatial Analytics | Esri. Retrieved April 25, 2023, from https://www.esri.com/en-us/home

Ewing, J. E., Jones, T. L., Pickens, J. F., Chastain-Howley, A., Dean, K. E., & Spear, A. A. (2004). Groundwater availability model for the Seymour Aquifer: Final report prepared for the Texas Water Development Board by INTERA.

Farooq, M., Park, S., Song, Y. S., Kim, J. H., Tariq, M., & Abraham, A. A. (2012). Subsurface cavity detection in a karst environment using electrical resistivity (er): A case study from yongweol-ri, South Korea. *Earth Sciences Research Journal*, *16*(1).

Fárová, K., Jelének, J., Kopačková-Strnadová, V., & Kycl, P. (2019). Comparing DInSAR and PSI techniques employed to Sentinel-1 data to monitor highway stability: A case study of a massive Dobkovičky landslide, Czech Republic. *Remote Sensing*, *11*(22).

Fehdi, C., Baali, F., Boubaya, D., & Rouabhia, A. (2011). Detection of sinkholes using 2d electrical resistivity imaging in the cheria basin (North–east of Algeria). *Arabian Journal of Geosciences*, *4*(1–2).

Ferretti, A., Monti-Guarnieri, A., Prati, C., & Rocca, F. (2007). Part B InSAR processing: a practical approach. In *InSAR Principles: Guidelines for SAR Interferometry Processing and Interpretation*.

Ferretti, A., Prati, C., & Rocca, F. (2001). Permanent scatterers in SAR interferometry. *IEEE Transactions on Geoscience and Remote Sensing*, *39*(1).

Filin, S., Avni, Y., Marco, S., & Baruch, A. (2006). Land degradation monitoring using airborne laser scanning. *ISPRS Archives*, *8*.

Foumelis, M., Blasco, J. M. D., Desnos, Y. L., Engdahl, M., Fernández, D., Veci, L., Lu, J., & Wong, C. (2018). ESA SNAP - Stamps integrated processing for Sentinel-1 persistent scatterer interferometry. *International Geoscience and Remote Sensing Symposium (IGARSS)*, *2018-July*.

Frumkin, A., Zaidner, Y., Na'aman, I., Tsatskin, A., Porat, N., & Vulfson, L. (2015). Sagging and collapse sinkholes over hypogenic hydrothermal karst in a carbonate terrain. Geomorphology, 229, 45-57.

Gambolati, G., & Teatini, P. (2021) Land Subsidence and its Mitigation. The Groundwater Project.

García Cook, A. (2021). 8. The Historical Importance of Tlaxcala in the Cultural Development of the Central Highlands. In *Supplement to the Handbook of Middle American Indians, Volume 1*.

Gebremichael, E., Sultan, M., Becker, R., el Bastawesy, M., Cherif, O., & Emil, M. (2018). Assessing Land Deformation and Sea Encroachment in the Nile Delta: A Radar Interferometric and Inundation Modeling Approach. *Journal of Geophysical Research: Solid Earth*, *123*(4).

Giampaolo, V., Capozzoli, L., Grimaldi, S., & Rizzo, E. (2016). Sinkhole risk assessment by ERT: The case study of Sirino Lake (Basilicata, Italy). *Geomorphology*, *253*.

Gili, J. A., Corominas, J., & Rius, J. (2000). Using Global Positioning System techniques in landslide monitoring. *Engineering geology*, 55(3), 167-192.

Goel, K., & Adam, N. (2014). A distributed scatterer interferometry approach for precision monitoring of known surface deformation phenomena. *IEEE Transactions on Geoscience and Remote Sensing*, *52*(9).

George, P. G., Mace, R. E., & Petrossian, R. (2011). Aquifers of Texas (Vol. 380, pp. 1-182). Austin, TX: Texas Water Development Board.

Gökkaya, E., Gutiérrez, F., Ferk, M., & Görüm, T. (2021). Sinkhole development in the Sivas gypsum karst, Turkey. *Geomorphology*, *386*.

Gustavson, T. C., Finley, R. J., & Baumgardner, R. W. (1981). Retreat of the Caprock Escarpment and denudation of the Rolling Plains in the Texas Panhandle. *BULL. ASSOC. ENG. GEOL.*, *18*(4).

Gutiérrez, F., Benito-Calvo, A., Carbonel, D., Desir, G., Sevil, J., Guerrero, J., Martínez-Fernández, A., Karamplaglidis, T., García-Arnay, Á., & Fabregat, I. (2019). Review on sinkhole monitoring and performance of remediation measures by high-precision leveling and terrestrial laser scanner in the salt karst of the Ebro Valley, Spain. In Engineering Geology (Vol. 248).

Gutiérrez, F., Cooper, A. H., & Johnson, K. S. (2008). Identification, prediction, and mitigation of sinkhole hazards in evaporite karst areas. *Environmental Geology*, *53*(5).

Gutiérrez, F., Galve, J. P., Lucha, P., Castañeda, C., Bonachea, J., & Guerrero, J. (2011). Integrating geomorphological mapping, trenching, InSAR and GPR for the identification and characterization of sinkholes: A review and application in the mantled evaporite karst of the Ebro Valley (NE Spain). *Geomorphology*, *134*(1–2).

Haley, M., Ahmed, M., Gebremichael, E., Murgulet, D., & Starek, M. (2022). Land Subsidence in the Texas Coastal Bend: Locations, Rates, Triggers, and Consequences. *Remote Sensing*, *14*(1).

Hanssen, R. F. (2001). Radar Interferometry: Data Interpretation and Error Analysis (Remote Sensing and Digital Image Processing). In *Springer*.

Harden, R. W. (1978). The Seymour aquifer, ground-water quality and availability in Haskell and Knox counties. Texas: Texas Department of Water Resources Rept, 226, 261.

Hatheway, A. W. (2005). Sinkholes and Subsidence: Karst and Cavernous Rocks in Engineering and Construction: (Tony Waltham, Fred Bell, and Martin Culshaw). *Environmental and Engineering Geoscience*, *11*(2).

Heidari, M., Khanlari, G. R., Taleb Beydokhti, A. R., & Momeni, A. A. (2011). The formation of cover collapse sinkholes in North of Hamedan, Iran. *Geomorphology*, *132*(3–4).

Henderson, T. (2012, June 12). Sinkhole in North Abilene growing larger, won't be repaired until July. National Post. https://www.bigcountryhomepage.com/news/sinkhole-in-north-abilene-growing-larger-wont-be-repaired-until-july/

Helz, R. L. (2021). InSAR—Satellite-based technique captures overall deformation "picture" | U.S. Geological Survey. Retrieved April 25, 2023, from https://www.usgs.gov/programs/VHP/insar-satellite-based-technique-captures-overall-deformation-picture

Hofierka, J., Gallay, M., Kaňuk, J., & Šašak, J. (2017). Modelling karst landscape with massive airborne and terrestrial laser scanning data. *Lecture Notes in Geoinformation and Cartography*.

Honings, J. P., Wicks, C. M., & Brantley, S. T. (2022). Ground-Penetrating Radar Detection of Hydrologic Connectivity in a Covered Karstic Setting. *Hydrology*, 9(10), 168.

Hooper, A., Bekaert, D., Spaans, K., & Arikan, M. (2012). Recent advances in SAR interferometry time series analysis for measuring crustal deformation. In *Tectonophysics* (Vols. 514–517).

Hooper, A., Segall, P., & Zebker, H. (2007). Persistent scatterer interferometric synthetic aperture radar for crustal deformation analysis, with application to Volcán Alcedo, Galápagos. Journal of Geophysical Research: Solid Earth, 112(B7).

Hooper, A., Zebker, H., Segall, P., & Kampes, B. (2004). A new method for measuring deformation on volcanoes and other natural terrains using InSAR persistent scatterers. Geophysical Research Letters, 31(23).

Hu, Y., Wang, F., Guin, C., & Zhu, H. (2018). A spatio-temporal kernel density estimation framework for predictive crime hotspot mapping and evaluation. *Applied Geography*, *99*.

Hussain, Y., Uagoda, R., Borges, W., Nunes, J., Hamza, O., Condori, C., Aslam, K., Dou, J., & Cárdenas-Soto, M. (2020). The potential use of geophysicalmethods to identify cavities, sinkholes and pathways forwater infiltration. *Water (Switzerland)*, *12*(8).

Hyndman, D., & Hyndman, D. (2016). Natural hazards and disasters. Cengage Learning.

Intrieri, E., Fontanelli, K., Bardi, F., Marini, F., Carlà, T., Pazzi, V., di Filippo, M., & Fanti, R. (2018). Definition of sinkhole triggers and susceptibility based on hydrogeomorphological analyses. Environmental Earth Sciences, 77(1).

Intrieri, E., Gigli, G., Nocentini, M., Lombardi, L., Mugnai, F., Fidolini, F., & Casagli, N. (2015). Sinkhole monitoring and early warning: An experimental and successful GB-InSAR application. *Geomorphology*, *241*.

Johnson, K. S. (2005). Subsidence hazards due to evaporite dissolution in the United States. *Environmental Geology*, 48(3).

Johnson, K. S. (1989). Development of the Wink Sink in west Texas, USA, due to salt dissolution and collapse. Environmental Geology and Water Sciences, 14, 81-92.

Johnson, K. S., Collins, E. W., & Seni, S. J. (2003). Sinkholes and land subsidence due to salt dissolution near Wink, West Texas, and other sites in western Texas and New Mexico. *Oklahoma Geological Survey Circular, 109*, 163-195.

Johnson, K. S., Land, L., Decker, D. D., & Hayman, N. W. (2021). Evaporite Karst in the Greater Permian Evaporite Basin (GPEB) of Texas, New Mexico, Oklahoma, Kansas, and Colorado. *Oklahoma Geological Survey Circular, 113*.

Jones, C. E., & Blom, R. G. (2014). Bayou Corne, Louisiana, sinkhole: Precursory deformation measured by radar interferometry. *Geology*, *42*(2).

Joyce, K. E., Samsonov, S. v., Levick, S. R., Engelbrecht, J., & Belliss, S. (2014). Mapping and monitoring geological hazards using optical, LiDAR, and synthetic aperture RADAR image data. In *Natural Hazards* (Vol. 73, Issue 2).

Keller, E. A., DeVecchio, D. E., & Clague, J. J. (2016). Natural hazards: Earth's processes as hazards, disasters, and catastrophes. In *Natural Hazards: Earth's Processes as Hazards, Disasters, and Catastrophes*.

Kersten, T., Kobe, M., Gabriel, G., Timmen, L., Schön, S., & Vogel, D. (2017). Geodetic monitoring of subrosion-induced subsidence processes in urban areas: Concept and status report. *Journal of Applied Geodesy*, *11*(1).

Kesaraju, S. (2012). A study of Ground Deformation over the Kiruna region using the StaMPS Technique. *Master Thesis*.

Khanlari, G., Heidari, M., Momeni, A. A., Ahmadi, M., & Beydokhti, A. T. (2012). The effect of groundwater overexploitation on land subsidence and sinkhole occurrences, western Iran. *Quarterly Journal of Engineering Geology and Hydrogeology*, *45*(4).

Kidanu, S., Varnavina, A., Anderson, N., & Torgashov, E. (2020). Pseudo-3D electrical resistivity tomography imaging of subsurface structure of a sinkhole—A case study in Greene County, Missouri. *AIMS Geosciences*, 6(1), 54-70.

Kim, J. W., Lu, Z., & Kaufmann, J. (2019). Evolution of sinkholes over Wink, Texas, observed by high-resolution optical and SAR imagery. *Remote Sensing of Environment*, *222*.

Kobal, M., Bertoncelj, I., Pirotti, F., Dakskobler, I., & Kutnar, L. (2015). Using lidar data to analyse sinkhole characteristics relevant for understory vegetation under forest cover - Case study of a high karst area in the Dinaric mountains. *PLoS ONE*, *10*(3).

Kpienbaareh, D., Sun, X., Wang, J., Luginaah, I., Kerr, R. B., Lupafya, E., & Dakishoni, L. (2021). Crop type and land cover mapping in northern malawi using the integration of sentinel-1, sentinel-2, and planetscope satellite data. *Remote Sensing*, *13*(4).

Kuniansky, E. L., Weary, D. J., & Kaufmann, J. E. (2016). The current status of mapping karst areas and availability of public sinkhole-risk resources in karst terrains of the United States. *Hydrogeology Journal*, *24*(3).

Latip, A. S. A., Matori, A. N., & Aobpaet, A. (2018). A Case Study on Offshore Platform Deformation Monitoring by using InSAR. *MATEC Web of Conferences*, *203*.

Lindsay, J. B. (2016). Efficient hybrid breaching-filling sink removal methods for flow path enforcement in digital elevation models. *Hydrological Processes*, *30*(6).

Liu, Y., Li, J., Fasullo, J., & Galloway, D. L. (2020). Land subsidence contributions to relative sea level rise at tide gauge Galveston Pier 21, Texas. *Scientific Reports*, *10*(1).

Liu, X. (2008). Airborne LiDAR for DEM generation: Some critical issues. In *Progress in Physical Geography* (Vol. 32, Issue 1).

Loke, M. H., & Barker, R. D. (1996). Rapid least-squares inversion of apparent resistivity pseudosections by a quasi-Newton method1. *Geophysical prospecting*, 44(1), 131-152.

Loke, M. H., Chambers, J. E., Rucker, D. F., Kuras, O., & Wilkinson, P. B. (2013). Recent developments in the direct-current geoelectrical imaging method. *Journal of Applied Geophysics*, *95*.

Maghsoudi, Y., van der Meer, F., Hecker, C., Perissin, D., & Saepuloh, A. (2018). Using PSInSAR to detect surface deformation in geothermal areas of West Java in Indonesia. *International Journal of Applied Earth Observation and Geoinformation*, *64*.

Mandal, D., Vaka, D. S., Bhogapurapu, N. R., Vanama, K. S. K., Kumar, V., Rao, Y. S., & Bhattacharya, A. (2019). Sentinel-1 SLC preprocessing workflow for polarimetric applications: A generic practice for generating dual-pol covariance matrix elements in SNAP S-1 Toolbox. *Preprints*, *November*.

Martel, R., Castellazzi, P., Gloaguen, E., Trépanier, L., & Garfias, J. (2018). ERT, GPR, InSAR, and tracer tests to characterize karst aquifer systems under urban areas: The case of Quebec City. *Geomorphology*, *310*.

Martinez, J. D., Johnson, K. S., & Neal, J. T. (1998). Sinkholes in evaporite rocks: surface subsidence can develop within a matter of days when highly soluble rocks dissolve because of either natural or human causes. American Scientist, 86(1), 38-51.

McGaughey, R. J., Andersen, H. E., & Reutebuch, S. E. (2006, April). Considerations for planning, acquiring, and processing LiDAR data for forestry applications. *In Proceedings of the 11th Biennial USDA Forest Service Remote Sensing Applications Conference*.

Memon, B. A., Patton, A. F., & Pitts, M. W. (1999). Control of naturally occurring brine springs and seeps in an evaporite karst setting. *Engineering geology*, 52(1-2), 83-91.

Modala, N. R., Ale, S., Goldberg, D. W., Olivares, M., Munster, C. L., Rajan, N., & Feagin, R. A. (2017). Climate change projections for the Texas High Plains and Rolling Plains. *Theoretical and Applied Climatology*, *129*(1–2).

Mohammady, M., Pourghasemi, H. R., Amiri, M., & Tiefenbacher, J. P. (2021). Spatial modeling of susceptibility to subsidence using machine learning techniques. *Stochastic Environmental Research and Risk Assessment*, *35*(8).

Montané, J. M. (2001). Geophysical Analysis of a Central Florida Karst Terrain using Light Detection and Ranging (LiDAR) and Ground Penetrating Radar (GPR) Derived Surfaces.

Monteiro, V. C., Miles, N. L., Richardson, S. J., Barkley, Z., Haupt, B. J., Lyon, D., ... & Davis, K. J. (2022). Methane, carbon dioxide, hydrogen sulfide, and isotopic ratios of methane observations from the Permian Basin tower network. *Earth System Science Data*, 14(5), 2401-2417.

Montgomery, J., Jackson, D., Kiernan, M., & Anderson, J. B. (2020). Use of geophysical methods for sinkhole exploration (No. 930-945). Auburn University. Highway Research Center.

Muhammad, F., Samgyu, P., Young, S. S., Ho Kim, J., Mohammad, T., & Adepelumi, A. A. (2012). Subsurface cavity detection in a karst environment using electrical resistivity (er): a case study from yongweol-ri, South Korea. *Earth Sciences Research Journal*, 16(1), 75-82.

Mukhwathi, U., & Fourie, F. (2020). The influence of angled survey lines on 2D ERT surveys using the Wenner (α) array with implications for groundwater exploration in Karoo rocks. *Journal of African Earth Sciences*, *168*.

Nam, B. H., Kim, Y. J., & Youn, H. (2020). Identification and quantitative analysis of sinkhole contributing factors in Florida's Karst. *Engineering Geology*, *271*.

Nart COŞKUN. (2012). The effectiveness of electrical resistivity imaging in sinkhole investigations. *International Journal of Physical Sciences*, *7*(15).

Nelson, W.J., Hook, R.W., Tabor, N. and Johnson, K.S., 2001. Clear Fork Group (Leonardian, Lower Permian) of north-central Texas. Oklahoma Geological Survey Circular, 104, pp.167-169.

Nelson, W.J., Hook, R. and Chaney, D., 2013. Lithostratigraphy of the lower Permian (Leonardian) clear fork formation of north-central Texas. The Carboniferous-Permian Transition: Bulletin 60, 60, p.286

Newton, J. G. (1987). Development of sinkholes resulting from man's activities in the Eastern United States. US Geological Survey Circular, 968.

Ng, A. H. M., Ge, L., & Li, X. (2015). Assessments of land subsidence in the Gippsland Basin of Australia using ALOS PALSAR data. Remote Sensing of Environment, 159.

Nof, R. N., Baer, G., Ziv, A., Raz, E., Atzori, S., & Salvi, S. (2013). Sinkhole precursors along the Dead Sea, Israel, revealed by SAR interferometry. Geology, 41(9).

Paine, J. G., Buckley, S. M., Collins, E. W., & Wilson, C. R. (2012). Assessing collapse risk in evaporite sinkhole-prone areas using microgravimetry and radar interferometry. *Journal of Environmental and Engineering Geophysics*, *17*(2).

Palanisamy Vadivel, S. K., Kim, D. J., Jung, J., Cho, Y. K., Han, K. J., & Jeong, K. Y. (2019). Sinking tide gauge revealed by space-borne InSAR: Implications for sea level acceleration at Pohang, South Korea. Remote Sensing, 11(3), 277.

Parvin, M., Hossain, S., & Rahman, A. (2019, January). Unsustainable groundwater depletion of Madhupur tract aquifer underneath Dhaka city and its relation to climate change. In International Conference on Sustainability in Natural and Built Environment (iCSNBE2019) (Vol. 19, p. 22).

Pawluszek-Filipiak, K., & Borkowski, A. (2020). Integration of DInSAR and SBAS techniques to determine mining-related deformations using Sentinel-1 data: The case study of rydultowy mine in Poland. *Remote Sensing*, *12*(2).

Pazzi, V., Di Filippo, M., Di Nezza, M., Carlà, T., Bardi, F., Marini, F., ... & Fanti, R. (2018). Integrated geophysical survey in a sinkhole-prone area: Microgravity, electrical resistivity tomographies, and seismic noise measurements to delimit its extension. *Engineering Geology*, 243, 282-293.

Pepe, A., & Calò, F. (2017). A review of interferometric synthetic aperture RADAR (InSAR) multi-track approaches for the retrieval of Earth's Surface displacements. In *Applied Sciences (Switzerland)* (Vol. 7, Issue 12).

Prats-Iraola, P., Rodriguez-Cassola, M., De Zan, F., Scheiber, R., López-Dekker, P., Barat, I., & Geudtner, D. (2015). Role of the orbital tube in interferometric spaceborne SAR missions. IEEE Geoscience and Remote Sensing Letters, 12(7), 1486-1490.

Price, R. D. (1978). Occurrence, quality, and availability of ground water in Jones county, Texas. Report 215 April 1978. 246 p, 40 fig, 12 tab, 60 ref.

Rajabi, A. (2018). Sinkhole Detection and Quantification Using LiDAR Data.

Ramirez, R., Lee, S. R., & Kwon, T. H. (2020). Long-term remote monitoring of ground deformation using sentinel-1 interferometric synthetic aperture radar (INSAR): Applications and insights into geotechnical engineering practices. *Applied Sciences (Switzerland)*, *10*(21).

Ritchie, J. C. (1995). Airborne laser altimeter measurements of landscape topography. *Remote Sensing of Environment*, *53*(2).

Rodriguez-Lloveras, X., Puig-Polo, C., Lantada, N., Gili, J. A., & Marturià, J. (2020). Two decades of GPS/GNSS and DInSAR monitoring of Cardona salt mines (NE of Spain) - natural and mining-induced mechanisms and processes. *Proceedings of the International Association of Hydrological Sciences*, *382*.

Rosen, P. A. (2000). Synthetic aperture radar interferometry. *Proceedings of the IEEE*, *88*(3).

Rucker, M. L., Panda, B. B., Meyers, R. A., & Lommler, J. C. (2013). Using InSAR to detect subsidence at brine wells, sinkhole sites, and mines. *Carbonates and Evaporites*, *28*(1–2).

Salvati, R., & Sasowsky, I. D. (2002). Development of collapse sinkholes in areas of groundwater discharge. *Journal of Hydrology*, *264*(1–4).

Saman, N., Heneghan, T., & Bou-Saada, T. E. (1996). Use of DOE-2 to Evaluate Evaporative Cooling in Texas Correctional Facilities.

Sato, H. P., Abe, K., & Ootaki, O. (2003). GPS-measured land subsidence in Ojiya City, Niigata Prefecture, Japan. *Engineering Geology*, *67*(3–4).

Seale, L. D., Florea, L. J., Vacher, H. L., & Brinkmann, R. (2008). Using ALSM to map sinkholes in the urbanized covered karst of Pinellas County, Florida - 1, Methodological considerations. *Environmental Geology*, *54*(5).

Shannon, J. C., Moore, D., Li, Y., & Olsen, C. (2019). LiDAR-based Sinkhole Detection and Mapping in Knox County, Tennessee. *Pursuit: The Journal of Undergraduate Research at the University of Tennessee*, *9*(1).

Shi, Y., Tang, Y., Lu, Z., Kim, J. W., & Peng, J. (2019). Subsidence of sinkholes in Wink, Texas from 2007 to 2011 detected by time-series InSAR analysis. *Geomatics, Natural Hazards and Risk*, *10*(1).

Sij, J., Morgan, C., Belew, M., Jones, D., & Wagner, K. (2008). Seymour aquifer water quality improvement project final report. Texas Water Resources Institute.

Sinkholes and subsidence: karst and cavernous rocks in engineering and construction. (2005). Choice Reviews Online, 42(10).

Stan-Kłeczek, I., Pierwoła, J., Marciniak, A., Sutkowska, K., & Tomaszewska, R. (2022). Multimethod geophysical investigation in karst areas: case studies from Silesia, Poland. *Bulletin of Engineering Geology and the Environment*, 81(6), 230.

Subedi, P., Subedi, K., Thapa, B., & Subedi, P. (2019). Sinkhole susceptibility mapping in Marion County, Florida: Evaluation and comparison between analytical hierarchy process and logistic regression based approaches. *Scientific Reports*, *9*(1).

Suh, J., & Choi, Y. (2017). Mapping hazardous mining-induced sinkhole subsidence using unmanned aerial vehicle (drone) photogrammetry. *Environmental Earth Sciences*, *76*(4).

Talib, O. C., Shimon, W., Sarah, K., & Tonian, R. (2022). Detection of sinkhole activity in West-Central Florida using InSAR time series observations. *Remote Sensing of Environment*, *269*.

Tesfaldet, Y. T., & Puttiwongrak, A. (2019). Seasonal groundwater recharge characterization using time-lapse electrical resistivity tomography in the the pkasattri watershed on Phuket Island, Thailand. *Hydrology*, *6(2)*.

Theron, A., Engelbrecht, J., Kemp, J., Kleynhans, W., & Turnbull, T. (2017). Detection of Sinkhole Precursors Through SAR Interferometry: Radar and Geological Considerations. *IEEE Geoscience and Remote Sensing Letters*, *14*(6).

Theron, A., & Engelbrecht, J. (2018). The role of earth observation, with a focus on SAR interferometry, for sinkhole hazard assessment. In *Remote Sensing* (Vol. 10, Issue 10).

Theron, A., Engelbrecht, J., Kemp, J., Kleynhans, W., & Turnbull, T. (2016). Detection of sinkhole precursors through SAR interferometry: First results from South Africa. *International Geoscience and Remote Sensing Symposium (IGARSS)*, *2016-November*.

Tzouvaras, M., Kouhartsiouk, D., Agapiou, A., Danezis, C., & Hadjimitsis, D. G. (2019). The use of Sentinel-1 synthetic aperture radar (SAR) images and open-source software for cultural heritage: An example from paphos area in Cyprus for mapping landscape changes after a 5.6 magnitude earthquake. *Remote Sensing*, *11*(15).

US Department of Agriculture. (2006). Land Resource Regions and Major Land Resource Areas of the United States, the Caribbean,and the Pacific Basin. *United States Department of AgricultureHandbook*, *296*.

USGS, 2018. Sinkholes completed. [accessed 2022 March 3]. https://www.usgs.gov/special-topics/water-science-school/science/sinkholes.

USGS. 2020. “Karst Map of the Conterminous United States - 2020 | U.S. Geological Survey.” 2020. https://www.usgs.gov/media/images/karst-map-conterminous-united-states-2020.

USGS - Pocket Texas Geology. (n.d.). Retrieved March 31, 2023, from https://txpub.usgs.gov/txgeology/

Vajedian, S., & Motagh, M. (2019). Extracting sinkhole features from time-series of TerraSAR-X/TanDEM-X data. *ISPRS Journal of Photogrammetry and Remote Sensing*, *150*.

Venter, Z. S., Barton, D. N., Chakraborty, T., Simensen, T., & Singh, G. (2022). Global 10 m Land Use Land Cover Datasets: A Comparison of Dynamic World, World Cover and Esri Land Cover. *Remote Sensing*, *14*(16).

Waltham, T. (2008). Sinkhole hazard case histories in karst terrains. *Quarterly Journal of Engineering Geology and Hydrogeology*, *41*(3).

Werner, C., Wegmüller, U., Strozzi, T., & Wiesmann, A. (2002, June). Processing strategies for phase unwrapping for INSAR applications. *In proceedings of the European conference on synthetic aperture radar (EUSAR 2002)* (Vol. 1, pp. 353-356).

Weary, D. J., & Doctor, D. H. (2016). Karst mapping in the United States: Past, present, and future. Special Paper of the Geological Society of America, 516.

White, W. B. (1984). Rate processes: chemical kinetics and karst landform development. *Groundwater as a Geomorphic Agent. Proc. Binghamton Symposia in Geomorphology: International Series 13, 1982*.

Winslow, A. G., & Doyel, W. W., 1954. Ground-water resources of Jones County, Texas. [Accessed 2022 July 5]. https://www.twdb.texas.gov/publications/reports/bulletins/doc/b5418.pdf.

Wiwattanachang, N., & Giao, P. H. (2011). Monitoring crack development in fiber concrete beam by using electrical resistivity imaging. *Journal of Applied Geophysics*, *75*(2).

Wood, M. K., & Blackburn, W. H. (1984). Vegetation and Soil Responses to Cattle Grazing Systems in the Texas Rolling Plains. *Journal of Range Management*, *37*(4).

Wu, Q., Deng, C., & Chen, Z. (2016). Automated delineation of karst sinkholes from LiDAR-derived digital elevation models. *Geomorphology*, *266*.

Xiao, H., Li, H., & Tang, Y. (2018). Assessing the effects of rainfall, groundwater downward leakage, and groundwater head differences on the development of cover-collapse and cover-suffosion sinkholes in central Florida (USA). *Science of the Total Environment*, *644*.

Xiao, X., Gutiérrez, F., & Guerrero, J. (2020). The impact of groundwater drawdown and vacuum pressure on sinkhole development. Physical laboratory models. *Engineering Geology*, *279*.

Xu, H., Chen, F., & Zhou, W. (2021). A comparative case study of MTInSAR approaches for deformation monitoring of the cultural landscape of the Shanhaiguan section of the Great Wall. *Heritage Science*, *9*(1)

Yague-Martinez, N., Prats-Iraola, P., Gonzalez, F. R., Brcic, R., Shau, R., Geudtner, D., Eineder, M., & Bamler, R. (2016). Interferometric Processing of Sentinel-1 TOPS Data. *IEEE Transactions on Geoscience and Remote Sensing*, *54*(4).

Yang, D., Qiu, H., Ma, S., Liu, Z., Du, C., Zhu, Y., & Cao, M. (2022). Slow surface subsidence and its impact on shallow loess landslides in a coal mining area. *Catena*, *209*.

Young, S. C. (2016). Identification of Potential Brackish Groundwater Production Areas--Gulf Coast Aquifer System. INTERA Incorporated.

Youssef, A. M., Al-Harbi, H. M., Gutiérrez, F., Zabramwi, Y. A., Bulkhi, A. B., Zahrani, S. A., Bahamil, A. M., Zahrani, A. J., Otaibi, Z. A., & El-Haddad, B. A. (2015). Natural and human-induced sinkhole hazards in Saudi Arabia: Distribution, investigation, causes and impacts. *Hydrogeology Journal*, *24*(3).

Zhang, S., Bogus, S., Baros, S., Neville, P., & Dow, R. (2019). Karst Sinkhole Detecting and Mapping Using Airborne LiDAR - A Conceptual Framework. *MATEC Web of Conferences*, *271*

Zhang, B., Wang, R., Deng, Y., Ma, P., Lin, H., & Wang, J. (2019). Mapping the Yellow River Delta land subsidence with multitemporal SAR interferometry by exploiting both persistent and distributed scatterers. *ISPRS Journal of Photogrammetry and Remote Sensing*, *148*.

Zhou, W., Beck, B. F., & Adams, A. L. (2002). Effective electrode array in mapping karst hazards in electrical resistivity tomography. *Environmental Geology*, *42*(8).

Zhou, W., & Beck, B. F. (2008). Management and mitigation of sinkholes on karst lands: an overview of practical applications. *Environmental Geology*, 55(4), 837-851.

Zhu, J., Taylor, T. P., Currens, J. C., & Crawford, M. M. (2014). Improved karst sinkhole mapping in Kentucky using LiDAR techniques: A pilot study in Floyds fork watershed. *Journal of Cave and Karst Studies*, *76*(3).

Zumpano, V., Pisano, L., & Parise, M. (2019). An integrated framework to identify and analyze karst sinkholes. *Geomorphology*, *332*. https://doi.org/10.1016/j.geomorph.2019.02.013

VITAE

Yosef Darge was born on May 9th, 1986, in Adama, Ethiopia. He earned a Bachelor's degree in Geoinformatics from Adama Science and Technology University in 2009, during which he participated in a range of projects focused on the practical application of spatial analysis techniques for landslide susceptibility, hazard zonation, and vulnerability assessment in the Ethiopian Rift Valley.

Following the successful completion of his Bachelor's degree, he began his professional career in a governmental organization in Ethiopia, where he progressed from a GIS researcher to a team leader, overseeing numerous projects. Driven by his passion for research and academic pursuits, he enrolled in a Master of Science program in GIS and Remote Sensing at Addis Ababa University in 2015, publishing his research findings in the prestigious International Journal of Applied Earth Observation and Geoinformation.

In August 2021, he was admitted to the graduate program in the Department of Geological Sciences at TCU, where he embraced new challenges and expanded his knowledge of surface and subsurface processes while delving into emerging concepts of InSAR. The program further equipped him with an in-depth understanding of the impact of various types of natural and human-induced disasters on human lives and critical infrastructure. Leveraging his expertise in GIS and remote sensing techniques, he explored the cause-and-effect relationships between these events.

With a relentless passion for research and a desire to make a significant impact in his field, he aims to pursue a doctoral program to further advance his knowledge and expertise in geoscience. His commitment to professional and academic development is unwavering, and he is dedicated to realizing his potential as a researcher and leader in his field.

ABSTRACT

EARLY SINKHOLE DETECTION AND CHARACTERIZATION IN WEST-CENTRAL TEXAS USING INSAR TIME SERIES AND ELECTRICAL RESISTIVITY TOMOGRAPHY

By Yosef Darge, MSc., 2023
Department of Geological Science
Texas Christian University

Thesis Advisor: Dr. Esayas Gebremichael, Assistant Professor of Geology

Sinkhole hazards pose a major threat to key infrastructure and human lives in Taylor, Fisher, Haskell, Knox, Stonewall, Callahan, and Jones Counties of the west-central region of Texas. These counties are underlain by soluble evaporite and carbonate rocks. In this study, a data fusion approach was adopted in which multi-source datasets and techniques were combined to detect and map the spatial distribution of sinkholes, quantify their displacement rates, and identify the processes and factors controlling their occurrence. (a) Using Light Detection and Ranging (LiDAR) datasets, areas with depressions ranging from 600 m^2 to 2600 m^2 and a CI value exceeding 0.86 were identified as potential sinkhole zones based on their morphological and physical characteristics. (b) deformation rates over the mapped depressions derived using Persistent Scatterer Interferometry technique applied on 56 level-1 Sentinel-1 images (2016 – 2021) and calibrated using long-term (2006 – 2021) GNSS. The result indicate that average and peak subsidence rates of -1.5 mm/yr and -6.5 mm/yr, respectively; (c) clusters of high subsidence rates were noted over are as underlain by evaporites belonging to the Clear Fork Group, and Blain Formation of carbonated rocks; (d) In order to investigate the formation of sinkholes in the highly vulnerable area of north Abilene, an Electrical Resistivity survey was conducted to identify their characteristics and underlying processes. In addition, groundwater level and discharge time series and other relevant datasets were integrated to assess the processes and factors that induce the formation of these features. Results of this study could be used to develop an early warning system

to implement mitigation strategies to curtail the impacts of the sinkhole hazards in Texas and other parts of the globe.